

The Influence of Submesoscales and Vertical Mixing on the Export of Sinking Tracers in Large-Eddy Simulations

JOHN R. TAYLOR, KATHERINE M. SMITH, AND CATHERINE A. VREUGDENHIL

*Department of Applied Mathematics and Theoretical Physics, University of Cambridge,
Cambridge, United Kingdom*

(Manuscript received 6 November 2019, in final form 12 February 2020)

ABSTRACT

We use idealized large-eddy simulations (LES) and a simple analytical theory to study the influence of submesoscales on the concentration and export of sinking particles from the mixed layer. We find that restratification of the mixed layer following the development of submesoscales reduces the rate of vertical mixing which, in turn, enhances the export rate associated with gravitational settling. For a neutral tracer initially confined to the mixed layer, subinertial (submesoscale) motions enhance the downward tracer flux, consistent with previous studies. However, the sign of the advective flux associated with the concentration of sinking particles reverses, indicating reentrainment into the mixed layer. A new theory is developed to model the gravitational settling flux when the particle concentration is nonuniform. The theory broadly agrees with the LES results and allows us to extend the analysis to a wider range of parameters.

1. Introduction

The flux of particulate organic carbon (POC) from the ocean surface layer into the interior, known as the “biological pump,” is a significant component of the global carbon cycle. It has been estimated that the carbon flux associated with the biological pump is between ~ 5 and 50 GtCyr^{-1} (Henson et al. 2011; Laws et al. 2000; Eppley and Peterson 1979). As illustrated in Fig. 1, the physical processes that influence the biological pump include the formation and breakup of aggregates (e.g., Burd and Jackson 2009), subduction by submesoscale currents (e.g., Omand et al. 2015), organization by mesoscale eddies (e.g., Waite et al. 2016), and resuspension by mixed layer turbulence (e.g., D’Asaro 2008). Here, we use idealized large-eddy simulations (LES) to study the influence of submesoscales and mixed layer turbulence on the export of sinking particles from the mixed layer.

Submesoscale currents with scales between roughly 1 and 10 km are ubiquitous features of the upper ocean (Thomas et al. 2008; McWilliams 2016). Submesoscales are known to induce large vertical circulations and enhance the exchange of tracers between the mixed layer

and ocean interior (Mahadevan and Tandon 2006; Klein and Lapeyre 2009). Often submesoscale currents are generated through various instabilities including mixed layer baroclinic instability (MLI) (e.g., Boccaletti et al. 2007; Fox-Kemper et al. 2008) and symmetric instability (e.g., Taylor and Ferrari 2009; Thomas 2005; Thompson et al. 2016), both of which ultimately increase the density stratification in the upper ocean and reduce the mixed layer depth (Fox-Kemper et al. 2008). For nutrient-replete mixed layers, when phytoplankton growth is limited by light exposure, the development of submesoscales can trigger phytoplankton blooms. This can occur either through a shoaling of the mixed layer and hence the depth of strong vertical mixing (Mahadevan et al. 2012), or when mixed layer restratification reduces the rate of vertical mixing within the mixed layer (Taylor and Ferrari 2011; Taylor 2016).

Based on data and observations from the North Atlantic Bloom Experiment, Omand et al. (2015) found that subduction of POC by submesoscale currents was a significant driver of export in the North Atlantic. They coupled a model for light-limited phytoplankton growth with an idealized physical model that was initialized with several zonal fronts and forced with an idealized seasonally varying wind stress and buoyancy flux [see also Mahadevan et al. (2012) for details of the physical model]. The horizontal resolution of the model (1 km)

Corresponding author: John R. Taylor, j.r.taylor@damtp.cam.ac.uk

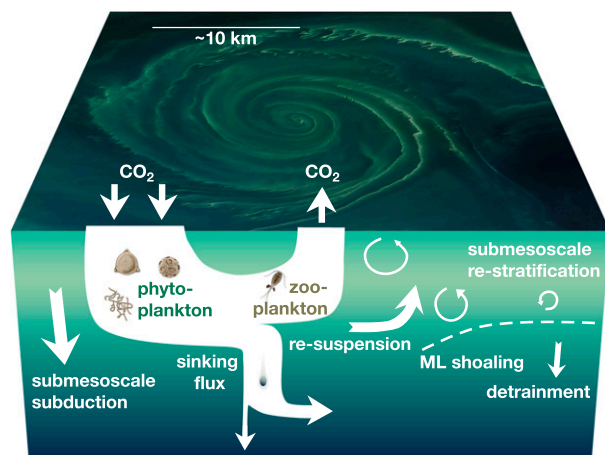


FIG. 1. Physical processes involved in the biological carbon pump. The schematic of the carbon pathways is adapted from Chisholm (2000). The top surface shows a false color image of a phytoplankton bloom in the Baltic Sea from *Landsat 8* and was obtained from earthobservatory.nasa.gov.

was such that three-dimensional turbulence in the mixed layer was not directly resolved. Instead, vertical mixing was parameterized using a depth-dependent turbulent diffusivity that was a prescribed function of the wind stress and the mixed layer depth, together with a convective adjustment scheme. As a result, the direct influence of submesoscales on small-scale turbulence within the mixed layer was not included in these simulations. Based on the model results and analysis of the observations, Omand et al. (2015) concluded that the submesoscale eddy-driven POC flux can account for up to half of the total POC export.

Liu et al. (2018) reached a similar conclusion by analyzing a 1-km resolution model and measurements from sediment traps in the Gulf of Mexico. They evaluated the export flux using several classes of Lagrangian particles that were advected with the model flow field and which sank at constant speeds varying from 20 to 100 m day⁻¹. They found that the simulated particles reached the depths of the sediment traps faster on average than they would through sinking alone. In other words, vertical advection of the particles enhanced export. The eddy field also induced large spatial variability in the distribution of particles which was reflected in the variability measured in the sediment traps.

Erickson and Thompson (2018) studied the export of POC using data collected from gliders during the OSMOSIS campaign in the northeast Atlantic. Although submesoscales are known to be active at this site (Thompson et al. 2016; Buckingham et al. 2016; Yu et al. 2019), Erickson and Thompson (2018) did not find evidence for substantial carbon export associated with subduction by submesoscales. They found that export

via subduction is sensitive to the strength of stratification in the pycnocline and concluded that more work was needed to quantify this export pathway in other locations.

In general, the surface mixed layer is a highly turbulent environment (e.g., Thorpe 2005). When turbulence maintains a uniform particle concentration within the mixed layer, the flux of particles out of the mixed layer can be reduced by vertical mixing (D'Asaro 2008). Following the arguments given in D'Asaro (2008), the homogeneous particle concentration within the mixed layer $C(t)$ satisfies

$$\frac{d}{dt}(Ch) = Cw_s, \quad (1)$$

where $h(t)$ is the mixed layer depth, w_s is the particle settling velocity, and turbulent entrainment at the base of the mixed layer has been neglected. Here $w_s < 0$, which corresponds to sinking particles. If the mixed layer depth is constant, Eq. (1) yields a mixed layer particle concentration that decays exponentially in time. Again following D'Asaro (2008), consider the following thought experiment: start with a uniform particle concentration, $C = C_0$ at $t = 0$. In the absence of turbulence the particle flux through the base of the mixed layer will be C_0w_s for $t < h/|w_s|$. After $t = h/|w_s|$ the particles will have left the mixed layer and the flux will drop to zero. In contrast, in the limit of strong vertical mixing and constant mixed layer depth, $C = C_0e^{w_s t/h}$. For $0 < t < h/|w_s|$, the particle flux is smaller than it would be in the absence of vertical mixing, and particles remain in the mixed layer after $t = h/|w_s|$.

During periods of mixed layer deepening, particles that had been recently exported from the mixed layer can be reentrained (D'Asaro 2008). Conversely, when the mixed layer depth becomes shallower (e.g., through increased solar insolation) it can leave behind particles which then experience lower levels of mixing and sink. Successive periods of deepening and shoaling of the mixed layer can enhance particle export through a process known as the “mixed layer pump” (Gardner et al. 1995; Bol et al. 2018; Dall’Omo et al. 2016).

The influence of turbulence in the ocean surface boundary layer on particle settling was studied using LES for a convectively forced mixed layer by Noh and Nakada (2010) and a wind-forced mixed layer with Langmuir circulations by Noh et al. (2006). In general, they found that turbulence can keep particles uniformly distributed in the mixed layer and that turbulence influences the export rate by controlling the rate of mixed layer deepening and through dynamics at the base of the mixed layer. However, neither of these studies included submesoscale processes.

We aim to examine the interactions between small-scale turbulence in the mixed layer and submesoscale dynamics and the influence of these physical processes on the concentration of sinking particles. To our knowledge, all previous studies of the influence of submesoscales on particle export have modeled small-scale turbulence either using a vertical diffusivity or a boundary layer turbulence model. This is an important distinction because existing boundary layer turbulence models [KPP, Price–Weller–Pinkel (PWP), Mellor–Yamada, etc.] do not account directly for the influence of submesoscales on turbulence and mixing. To overcome this problem we use LES which, by definition, resolve the largest and most energetic turbulent overturning motions. The advantage of this approach is that our simulations capture the dynamical interactions between boundary layer turbulence and submesoscales.

The obvious disadvantage of this approach is its computational cost. As described in the next section, the resolution of our simulations is several meters and computational constraints limit our horizontal domain size to 4 km. As we will show, the computational domain is nevertheless large enough to capture the development of several submesoscale eddies which eventually merge into a single eddy that fills our domain. We are not able to resolve interactions between mature submesoscale eddies or the influence of mesoscale currents. However these restrictions can provide useful information; by excluding mesoscale (and larger scale) motions, our simulations can be used to isolate the influence of submesoscales on sinking tracers, albeit in an idealized geometry.

Here, we identify a new mechanism leading to enhanced export of sinking particles. Specifically, we find that the restratification of the mixed layer by submesoscales inhibits the rate of vertical mixing in the mixed layer which enhances the export flux. For particles that sink faster than $\sim 10 \text{ m day}^{-1}$, mixing is unable to maintain a uniform particle concentration in the mixed layer, and the concentration becomes larger at the base of the mixed layer. As a result, the sinking flux of particles is enhanced compared to what it would be in the absence of submesoscales. This mechanism is distinct from the more direct subduction of particles due to submesoscale currents seen by previous authors (Omand et al. 2015; Liu et al. 2018). While we also see large vertical velocities associated with the submesoscales, in our simulations the suppression of small-scale turbulence plays a more important role. The relative importance of these effects likely depends on specific conditions and parameters and we leave a comparison of these processes for other conditions to a future study.

In section 2 we develop an extension to the theory described in D’Asaro (2008) to account for incomplete mixing and nonuniform particle concentration. The theory yields a prediction for the export rate as a function of the particle sinking speed and the turbulent diffusivity. For sufficiently weak mixing the predicted export rate increases, in quantitative agreement with the export rate diagnosed from the LES.

2. Theory for enhanced export due to incomplete mixing

Before describing the results of the LES, we will first describe a simple theory to show that weak vertical mixing can enhance the export rate of sinking particles from the mixed layer. We will then use this framework to analyze the LES where restratification induced by submesoscale instabilities inhibits the rate of vertical mixing. Although our focus is on the influence of submesoscales on POC export, the theory presented here is more general and could be used to analyze other instances when vertical mixing is relatively weak, for example, during periods of weak forcing, or when the net surface heat flux or Ekman buoyancy flux is stabilizing. A similar framework could also be used to study buoyant particles, although some assumptions might need to be revisited.

The theory presented here can be viewed as an extension to D’Asaro (2008) where now the particle concentration is allowed to vary in the vertical direction. The theory yields a prediction for the export rate as a function of the particle sinking speed, mixed layer depth, and turbulent mixing rate. We model turbulent mixing using a vertical diffusivity with the caveat that this might not be the most accurate representation of the effects of turbulence, particularly in the case of convection where scalar fluxes can be highly nonlocal (Large et al. 1994). In section 4c we will test the model using the turbulent diffusivity and export rates diagnosed from the LES.

Here, we model the concentration of sinking particles $c(x, y, z, t)$ using a continuum approximation. We assume that the particles sink with a prescribed settling velocity and we neglect interactions between particles (e.g., aggregation, breakup, and remineralization). With these assumptions, the particle concentration is modeled using an advection–diffusion equation of the form

$$\frac{\partial c}{\partial t} + \mathbf{u} \cdot \nabla c + w_s \frac{\partial c}{\partial z} = \kappa \nabla^2 c, \quad (2)$$

where \mathbf{u} is the fluid velocity, κ is a diffusion coefficient, and w_s is the particle settling velocity. By convention we

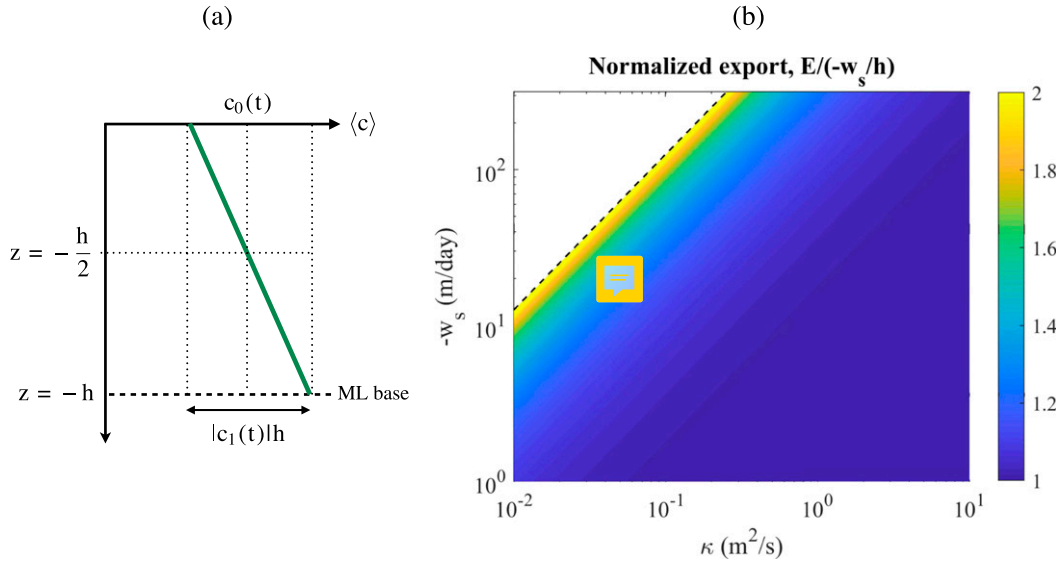


FIG. 2. (a) Sketch of the variables used in the theory presented in section 2. The mixed layer depth is denoted h , c_0 is the mean particle concentration in the mixed layer, and the change in particle concentration across the mixed layer is given by $|c_1|/h$. Note that the profile shown is for $c_1 < 0$. (b) Steady-state export rate predicted by the theory and normalized by $-w_s/h$, the export rate for a homogeneous particle concentration. The dashed black line shows $T \equiv \kappa/(w_s h) = (1 - \sqrt{8})/8$, and no steady-state solution exists above this line. A mixed layer depth of $h = 300$ m was used to calculate the predicted export rate E .

take $w_s < 0$ so that the particles move down relative to the fluid. A similar approach is often used to simulate sinking particles in biogeochemical models (e.g., Resplandy et al. 2019).

We can construct a one-dimensional model for the mean tracer concentration by averaging Eq. (2) over a given horizontal area. If we neglect the mean horizontal tracer fluxes, the mean tracer concentration $\bar{c}(z, t)$ satisfies

$$\frac{\partial \bar{c}}{\partial t} + \frac{\partial}{\partial z}(w_s \bar{c}) = \frac{\partial}{\partial z} \left(\kappa_T \frac{\partial \bar{c}}{\partial z} \right), \quad (3)$$

where we have assumed that w_s is constant and

$$\kappa_T \equiv \kappa - \frac{\overline{w'c'}}{\partial \bar{c} / \partial z} \quad (4)$$

is the total vertical diffusivity, including the turbulent and diffusive components.

We then model the mean tracer concentration in the mixed layer as the sum of a constant term and a term with a linear depth dependence:

$$\bar{c}(z, t) = c_0(t) + c_1(t) \left(z + \frac{h}{2} \right), \quad (5)$$

where h is the mixed layer depth. As sketched in Fig. 2a, the constants are set such that c_0 is the mean tracer concentration at the center of the mixed layer, and

$c_0 + c_1 h/2$ and $c_0 - c_1 h/2$ are the mean tracer concentrations at the top and bottom of the mixed layer, respectively. Representing the mean tracer concentration as the sum of a constant and linear term is equivalent to keeping the first two terms in a Taylor series expansion. Therefore, we anticipate that this approximation will work well when departures away from a uniform tracer concentration are small. However, as we will show, this approximation appears to produce a reasonable match to the mean tracer profiles simulated with the LES, even for rapidly sinking tracers where the change in tracer concentration across the mixed layer is large. We do not assume that the concentration is necessarily higher at the mixed layer base, but as we will show, this follows from the model solution when $w_s < 0$.

Integrating Eq. (3) over the mixed layer depth gives

$$\int_{-h}^0 \frac{dc_0}{dt} dz - w_s c_0 + w_s c_1 \frac{h}{2} = \kappa_T|_{z=-h} c_1, \quad (6)$$

where we set $w_s = 0$ and $\kappa_T = 0$ at $z = 0$. For simplicity, we will neglect reentrainment of particles into the mixed layer and deepening of the mixed layer base. With the assumption that h is constant in time and that $\kappa_T|_{z=-h} = 0$ (consistent with the assumption of no entrainment through the base of the mixed layer), Eq. (6) becomes

$$h \frac{dc_0}{dt} - w_s c_0 = -w_s c_1 \frac{h}{2}. \quad (7)$$

For a well-mixed tracer profile, $c_1 = 0$, and Eq. (7) will yield an exponentially decaying tracer concentration in the mixed layer, consistent with D'Asaro (2008).

When $c_1 \neq 0$, we need another equation to close the model. Taking the difference between the integrated tracer budget in the top and bottom halves of the mixed layer, that is,

$$\int_{-h/2}^0 (3) dz - \int_{-h}^{-h/2} (3) dz, \quad (8)$$

and again setting $dh/dt = \kappa_T|_{z=-h} = 0$ gives

$$\frac{h^2}{4} \frac{dc_1}{dt} - w_s c_0 - w_s c_1 \frac{h}{2} = -2\kappa_T|_{-h/2} c_1. \quad (9)$$

Equations (7) and (9) form a closed system which can be solved for $c_0(t)$ and $c_1(t)$. Later, in section 4c we will time-step these equations with a time-dependent κ_T for comparison with results from an LES model.

If we make the further assumption that $\kappa_T|_{-h/2}$ is constant in time (and use κ_0 to denote this constant), then we can obtain analytical solutions to Eqs. (7) and (9). First, it is useful to rewrite Eqs. (7) and (9) in matrix form:

$$\begin{pmatrix} \frac{dc_0}{dt} \\ \frac{dc_1}{dt} \end{pmatrix} = \begin{pmatrix} \frac{w_s}{h} & -\frac{w_s}{2h} \\ \frac{4w_s}{h^2} & 2 - \frac{8\kappa_0}{h^2} \end{pmatrix} \begin{pmatrix} c_0 \\ c_1 \end{pmatrix}. \quad (10)$$

If κ_0 , h , and w_s are constant in time, these equations have solutions of the form

$$\begin{pmatrix} c_0 \\ c_1 \end{pmatrix} = A \mathbf{v}_{(+)} e^{\lambda_{(+)} t} + B \mathbf{v}_{(-)} e^{\lambda_{(-)} t}, \quad (11)$$

where $\mathbf{v}_{(\pm)}$ and $\lambda_{(\pm)}$ are the eigenvectors and eigenvalues of the coefficient matrix on the right-hand side of Eq. (10). In this case, the eigenvalues and eigenvectors can be written

$$\lambda_{(\pm)} = \frac{3w_s}{2h} - \frac{4\kappa_0}{h^2} \pm \frac{\sqrt{(8\kappa_0 - hw_s)^2 - 8h^2w_s^2}}{2h^2}, \quad (12)$$

and

$$\mathbf{v}_{(\pm)} = \begin{bmatrix} \frac{3h}{8} - \frac{\kappa_0}{w_s} \pm \frac{\sqrt{(8\kappa_0 - hw_s)^2 - 8h^2w_s^2}}{8w_s} \\ 1 \end{bmatrix}. \quad (13)$$

When $8\kappa_0 > (1 - \sqrt{8})hw_s$, both eigenvalues are real and negative and since $w_s < 0$ the solutions will decay

exponentially in time. In this case, the rate of decay will approach the largest eigenvalue. In the limit of strong mixing, that is, $\kappa_0 \gg |w_s|h$, the largest eigenvalue is $\lambda \simeq w_s/h$, which matches the exponential decay rate from D'Asaro (2008). Similarly, in the limit of strong mixing, $c_0 \gg c_1h$, implying that the concentration is nearly uniform in the mixed layer. Our model can, therefore, be viewed as a generalization of D'Asaro (2008) to allow for nonuniform particle concentration resulting from incomplete mixing.

When $8\kappa_0 < (1 - \sqrt{8})hw_s$, the solutions become complex with a nonzero imaginary part. In this case, mixing is too weak to keep the particles suspended in the mixed layer and the modeled particle concentration will become zero in a finite time. After this time, the modeled particle concentration becomes negative and the model breaks down. As discussed by D'Asaro (2008), in the absence of advection and mixing all particles will sink out of a layer of thickness h in a time $h/|w_s|$. Our model gives a prediction of the minimum mixing required to prevent the particle concentration from reaching zero in a finite time.

It is also useful to quantify the degree of nonuniformity in the mixed layer particle concentration, particularly since this quantity might be more readily testable using observations than the export rate. To do this, we can define the ratio of the mean particle concentration to the change in the particle concentration across the mixed layer,

$$r \equiv \frac{\frac{1}{h} \int_{-h}^0 \bar{c} dz}{\bar{c}_{z=0} - \bar{c}_{z=-h}}. \quad (14)$$

For our model with $\bar{c} = c_0 + c_1(z + h/2)$, this becomes

$$r = \frac{c_0}{c_1 h}. \quad (15)$$

Equations (7) and (9) can be combined to give the following nonlinear first-order differential equation for $r(t)$:

$$\frac{dr}{dt} = -\frac{w_s}{h} \left[4r^2 + r \left(1 - \frac{8\kappa_T}{w_s h} \right) + \frac{1}{2} \right]. \quad (16)$$

Since the right hand side of Eq. (16) is quadratic in r , there are two steady solutions with $dr/dt = 0$:

$$r = T - \frac{1}{8} \pm \sqrt{T^2 - T/4 - 7/64}, \quad (17)$$

where $T \equiv \kappa_0/(w_s h)$ is the ratio of the turbulent diffusivity to the product of the sinking speed and the mixed layer depth. This ratio has a natural interpretation if the

mixing length hypothesis is invoked to express the turbulent diffusivity as the product of a turbulent velocity scale, w_* , and a mixing length that can be taken to be the mixed layer depth. Then $T = w_*/w_s$ is the ratio of the turbulent velocity scale to the sinking speed. For sinking particles with $w_s < 0$, real, steady solutions for r require $T < (1 - \sqrt{8})/8$, which is consistent with the requirement for real eigenvalues. In other words, **the turbulent velocity scale must exceed the settling speed (multiplied by an $O(1)$ constant) in order for the particles to remain suspended in the mixed layer.**

The ratio r can also be related to the surface concentration. For our model tracer profile

$$\frac{\bar{c}|_{z=0}}{\frac{1}{h} \int_{-h}^0 \bar{c} dt} = 1 + \frac{c_1 h}{2c_0} = 1 - \frac{1}{2r}. \quad (18)$$

Since the tracer concentration must remain positive ($\bar{c} > 0$) and $r < 0$, the model requires $r < -1/2$.

Finally, we can use the model solutions to obtain an expression for the export rate. First, define the export rate in terms of the integrated mixed layer tracer concentration

$$E \equiv \frac{-\frac{d}{dt} \int_{-h}^0 \bar{c} dz}{\int_{-h}^0 \bar{c} dz}, \quad (19)$$

which in our model is

$$E = -\frac{dc_0/dt}{c_0}. \quad (20)$$

In the limit of a well-mixed tracer with $c_0 = Ae^{w_s t/h}$, E is the rate of exponential decay of the mixed layer particle concentration, that is, $E = -w_s/h$. Using Eq. (7), the export rate can be written

$$E = -\frac{w_s}{h} + \frac{w_s c_1}{2c_0} = -\frac{w_s}{h} \left(1 - \frac{1}{2r} \right). \quad (21)$$

For sinking tracers with $w_s < 0$ and $r < 0$, the export rate is enhanced by a factor of $1 + 1/(2|r|)$ due to incomplete mixing. The normalized export rate is shown in Fig. 2 as a function of κ_0 and w_s for a mixed layer depth of $h = 300$ m. The dashed black line in this panel corresponds to $\kappa_0 = w_s h(1 - \sqrt{8})/8$ [or equivalently $T = (1 - \sqrt{8})/8$]. Steady solutions do not exist in the white region above this line where $\kappa < w_s h(1 - \sqrt{8})/8$ and mixing is unable to compete with gravitational settling. Although steady solutions do not exist in this region, Eqs. (7) and (9) will still yield a prediction for the time evolution of the particle

concentration and export rate. These predictions will be tested in section 4c using large-eddy simulations.

3. Numerical methods

In this section, we introduce the numerical methods that will be used for the large-eddy simulations discussed below in section 4. The large-eddy simulations solve the filtered incompressible Navier–Stokes momentum equation under the Boussinesq approximation

$$\frac{\partial \bar{\mathbf{u}}}{\partial t} + \bar{\mathbf{u}} \cdot \nabla \bar{\mathbf{u}} = -\frac{1}{\rho_0} \nabla \bar{p} + \bar{b} \mathbf{k} + \nu \nabla^2 \bar{\mathbf{u}} - \nabla \cdot \boldsymbol{\tau}, \quad (22)$$

where p is pressure, ρ_0 is the reference density, and \mathbf{k} is the unit vector in the vertical direction. The overbar in Eq. (22) represents an implicit low-pass filter, where the filter width is the grid scale. The subgrid-scale contributions are taken into account through the subfilter stress tensor $\boldsymbol{\tau}_{ij} = \bar{u}_i \bar{u}_j - \bar{u}_i \bar{u}_j$, where Einstein summation is implied. The deviatoric part of the stress tensor $\boldsymbol{\tau}_{ij}^d$ is modeled as

$$\boldsymbol{\tau}_{ij}^d = \boldsymbol{\tau}_{ij} - \frac{1}{3} e_{ij} \tau_{kk} = -2\nu_{\text{SGS}} \bar{S}_{ij}, \quad (23)$$

where e_{ij} is the delta function, ν_{SGS} is the subgrid-scale eddy viscosity, and $\bar{S}_{ij} = (1/2)[\partial_i \bar{u}_j(x, t) + \partial_j \bar{u}_i(x, t)]$ is the resolved rate-of-strain tensor. The subgrid-scale viscosity ν_{SGS} is modeled with the anisotropic minimum dissipation (AMD) model which is described in section 3a. To simplify the notation, we will omit the overbar from all variables below.

The **initial conditions and forcing applied to each simulation are illustrated in Fig. 3.** Simulation A has a background horizontal buoyancy gradient (see below for implementation) and a 4-km domain size in both horizontal directions. Simulation B does not have a background horizontal buoyancy gradient and as a result, submesoscales do not develop. To reduce the computational cost, the horizontal domain size is 2 km in Simulation B. All other aspects of the simulations are identical. Both simulations are forced by applying a constant negative buoyancy flux at the top of the domain. Simulation A includes submesoscales and small-scale turbulence, while Simulation B only includes turbulent convection. The wind stress is set to zero in both simulations.

The computational domain is discretized using 1024 gridpoints in both horizontal directions in Simulation A and 512 gridpoints in Simulation B such that the horizontal resolution is 3.9 m in both cases. Both simulations use 257 gridpoints in the vertical direction with a resolution of 3.1 m.

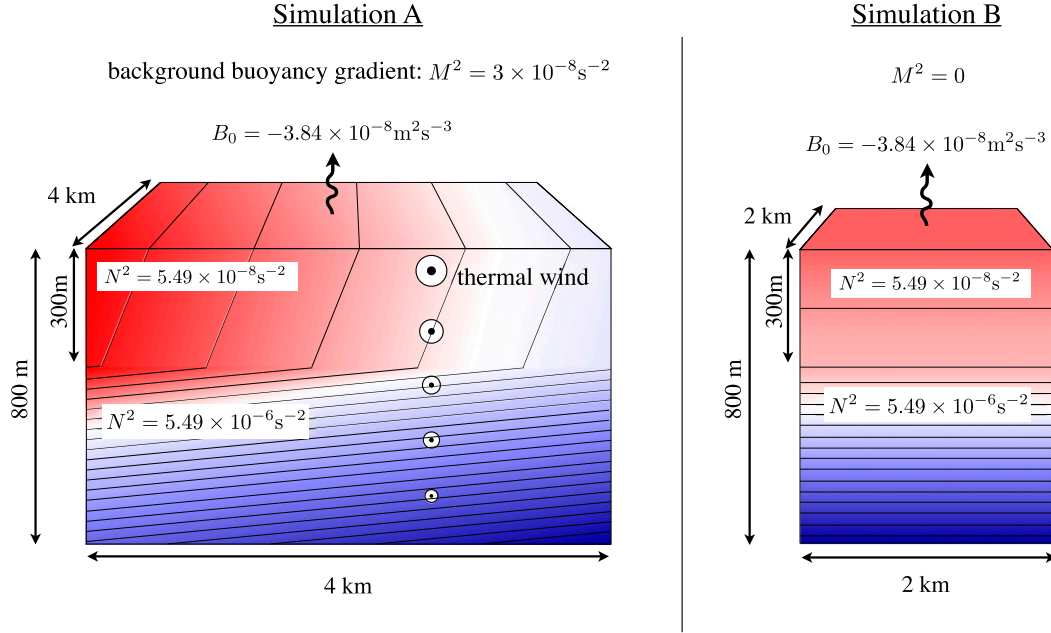


FIG. 3. Schematic of the initial conditions and forcing applied to the LES.

The initial conditions are broadly inspired by conditions in late winter/early spring of the North Atlantic as observed during the North Atlantic Bloom Experiment (e.g., Fennel et al. 2011; Mahadevan et al. 2012; Omand et al. 2015). Specifically, the simulations start with a weakly stratified layer with a thickness of 300 m overlying a deeper strongly stratified pycnocline with a thickness of 500 m. The squared buoyancy frequency in the upper layer is $N^2 = 5.5 \times 10^{-8} \text{ s}^{-2}$, while in the lower layer it is $N^2 = 5.5 \times 10^{-6} \text{ s}^{-2}$ and the stratification is initially constant in each layer. The Coriolis parameter is $f = 1.28 \times 10^{-4} \text{ s}^{-1}$, corresponding to a latitude of 61.65°N .

The simulations use periodic boundary conditions in both horizontal directions. Free-slip (no stress), rigid lid boundary conditions are applied at the top and bottom of the computational domain, that is,

$$\frac{\partial u}{\partial z} = \frac{\partial v}{\partial z} = w = 0, \quad \text{at } z = -800 \text{ m}, 0. \quad (24)$$

The computational domain in each simulation can be thought of as an idealized representation of a small patch of open ocean, albeit without any direct influence from larger-scale variability. A constant buoyancy flux, $B_0 = -3.84 \times 10^{-8} \text{ m}^2 \text{ s}^{-3}$, is applied to the top of the domain, while the vertical buoyancy gradient at the bottom of the domain matches the initial value of N^2 . The surface buoyancy flux is constant in space and time and corresponds to a surface heat flux of about -150 W m^{-2} (using a thermal expansion coefficient $\alpha = 1.1 \times 10^{-4} \text{ }^\circ\text{C}^{-1}$

and heat capacity $c_p = 4 \times 10^3 \text{ J kg}^{-1} \text{ }^\circ\text{C}^{-1}$). In the absence of mixed layer restratification, the surface buoyancy flux will drive sustained turbulent convection.

We assume a linear equation of state and solve a single conservation equation for the changes in buoyancy with respect to an arbitrary reference value. In Simulation A the total buoyancy b_T is decomposed into a background gradient M^2 and departures from this gradient,

$$b_T = M^2 x + b. \quad (25)$$

Using this decomposition in the buoyancy conservation equation gives

$$\frac{\partial b}{\partial t} + \mathbf{u} \cdot \nabla b + u M^2 = \nabla \cdot [(\kappa + \kappa_{b,\text{SGS}}) \nabla b], \quad (26)$$

where \mathbf{u} is the resolved velocity from the LES and $\kappa_{b,\text{SGS}}$ represents the contribution from the subgrid-scale model to the buoyancy diffusivity (described below). The simulations solve Eq. (26) subject to periodic horizontal boundary conditions. This “frontal zone” configuration has been used in a number of previous studies of submesoscale dynamics (e.g., Taylor and Ferrari 2010; Thomas et al. 2016; Taylor 2016, 2018). It is assumed that M^2 is constant, although the local horizontal buoyancy gradient can vary through changes in b . This assumption, together with periodic boundary conditions applied to b , is equivalent to imposing a constant difference in total buoyancy across the domain such that $b_T(0, y, z, t) - b_T(L_x, y, z, t) = M^2 L_x$, where L_x is the horizontal domain

size. The background horizontal buoyancy gradient is $M^2 = 3 \times 10^{-8} \text{ s}^{-2}$ in Simulation A and $M^2 = 0$ in Simulation B.

As discussed in Mahadevan et al. (2010) and Mahadevan et al. (2012), the destabilizing surface buoyancy flux can be compared with the anticipated restratification induced by MLI using the following ratio

$$R_{\text{MLI}} = \frac{B_0 f}{M^4 h^2}. \quad (27)$$

Note that this ratio was first defined by Mahadevan et al. (2010) with a scaling factor of 0.06 in the denominator. However, recent work (Taylor 2016; Callies and Ferrari 2018; Taylor 2018) has found that stable stratification develops in the mixed layer for $R_{\text{MLI}} \leq 1$ without the scaling factor. With the parameters for Simulation A, $R_{\text{MLI}} = 1$, and we anticipate that the mixed layer will restratify despite the persistent surface buoyancy loss at the top boundary.

The particle concentration is modeled by solving equations of the form

$$\frac{\partial c}{\partial t} + \mathbf{u} \cdot \nabla c + w_s \frac{\partial c}{\partial z} = \nabla \cdot [(\kappa + \kappa_{\text{c,SGS}}) \nabla c], \quad (28)$$

where $w_s < 0$ is the settling velocity and $\kappa_{\text{c,SGS}}$ is the subgrid-scale contribution to the diffusivity of the particle concentration. The settling velocity depends on the size, shape, and density of the sinking particles and can vary from -1 m day^{-1} for individual phytoplankton cells to over -100 m day^{-1} for marine snow aggregates (e.g., Burd and Jackson 2009).

Here, we simulate the concentration of particles with four settling velocities, $w_s = 0, -10, -50$, and -100 m day^{-1} . The concentration of particles with each settling velocity is calculated by solving Eq. (28). The settling velocity of each class of particles is assumed to be constant and the particle classes do not interact. In other words, we neglect the aggregation, breakup, and remineralization of the particles. Neglecting these factors is likely not justified, but it greatly simplifies the analysis and allows us to focus on the physical mechanisms controlling the export of sinking particles.

No flux boundary conditions are applied to the particle concentration fields. This is done by setting $\partial c / \partial z = 0$ at the top and bottom of the domain to ensure that the diffusive flux vanishes. The settling velocity is also set to zero at the top and bottom boundaries. This causes a slight accumulation of particles at the bottom boundary in the simulation with $w_s = -100 \text{ m day}^{-1}$, but this does not influence the export from the mixed layer.

The flow in each simulation is allowed to develop for 26 h before the particle concentration equations are

initialized and time stepped. This allows small-scale turbulence to develop throughout the mixed layer and prevents a large export event associated with the spinup of the model. The particle concentration is initialized with a constant value in the mixed layer with no particles in the thermocline. Although highly idealized, this is intended to mimic an injection of particles into the mixed layer as might happen for example at the end of a phytoplankton bloom. Smith et al. (2016) recently found that the vertical flux of passive tracers is sensitive to the initial distribution, but we do not explore this dependence here. Since Eq. (28) is linear in c , the particle concentration can be scaled by an arbitrary constant. Here without loss of generality, we set the initial particle concentration to 1 in the mixed layer. Specifically, the particle concentration is initialized at $t = 26$ hours using a one-dimensional profile:

$$c = \frac{1}{2} \left[1 + \tanh \left(\frac{z + 300 \text{ m}}{20 \text{ m}} \right) \right]. \quad (29)$$

Subgrid-scale model

The subgrid-scale eddy viscosity ν_{SGS} and the subgrid-scale eddy diffusivities $\kappa_{b,\text{SGS}}$ in Eq. (26) and $\kappa_{c,\text{SGS}}$ in Eq. (28) are calculated using the AMD model (Rozema et al. 2015). The AMD model has been used in stratified boundary layers by Abkar et al. (2016), Abkar and Moin (2017), and Vreugdenhil and Taylor (2018). The AMD parameterization is well suited to flows with turbulent and laminar regions since the eddy viscosity and diffusivity tend to be small in regions where there is little turbulence. The accuracy of the AMD model has been found to be similar to that of the dynamic Smagorinsky method (Vreugdenhil and Taylor 2018). However, the AMD model has the advantage of being simpler to incorporate into parallelized numerical codes because the subgrid-scale calculation only relies on local gradient values and no averaging is required. Here, we also apply the Verstappen (2018) requirement of normalizing the velocity vector and gradients by the filter width, to counteract any spurious kinetic energy transferred by the advection term in the momentum equations.

The subgrid-scale eddy viscosity associated with the AMD model can be written

$$\nu_{\text{SGS}} = (C\delta)^2 \frac{\max\{-(\hat{\partial}_k \hat{u}_i)(\hat{\partial}_k \hat{u}_j) \hat{S}_{ij}, 0\}}{(\hat{\partial}_l \hat{u}_m)(\hat{\partial}_l \hat{u}_m)}, \quad (30)$$

where $\hat{S}_{ij} = (1/2)(\hat{\partial}_i \hat{u}_j + \hat{\partial}_j \hat{u}_i)$ and $\hat{\partial}_i \hat{u}_j = (\delta_i / \delta_j) \partial_i u_j$. The subgrid-scale eddy diffusivities are

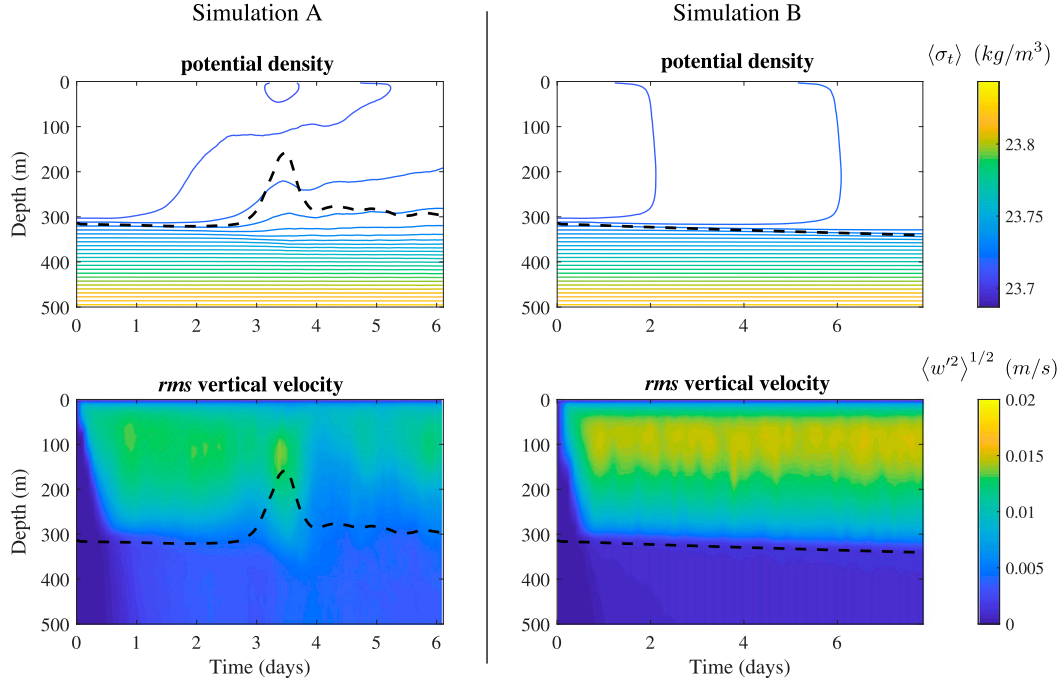


FIG. 4. Contours of the horizontally averaged (top) potential density and (bottom) rms vertical velocity for (left) Simulation A and (right) Simulation B. The black dashed line shows the mixed layer depth defined as the depth where the horizontally averaged density is 0.01 kg m^{-3} larger than the surface.

$$\kappa_{b,\text{SGS}} = (C\delta)^2 \frac{\max\{-(\partial_k \hat{u}_i)(\partial_k b)\partial_i b, 0\}}{(\partial_l b)(\partial_l b)},$$

$$\kappa_{c,\text{SGS}} = (C\delta)^2 \frac{\max\{-(\partial_k \hat{u}_i)(\partial_k c)\partial_i c, 0\}}{(\partial_l c)(\partial_l c)}, \quad (31)$$

where $\hat{\partial}_i b = \delta_i \partial_i b$ and $\hat{\partial}_i c = \delta_i \partial_i c$. For the filter width δ we follow the suggestion by Verstappen (2018) to use

$$\frac{1}{\delta^2} = \frac{1}{3} \left(\frac{1}{\delta_1^2} + \frac{1}{\delta_2^2} + \frac{1}{\delta_3^2} \right), \quad (32)$$

with the modified Poincaré constant $C^2 = 1/12$ and δ_i where $i = 1, 2, 3$ are the widths of the grid cells in x, y, z directions, respectively.

4. Results

a. Qualitative description

In both simulations, turbulent convection develops quickly in response to the surface buoyancy loss. Convection erodes the weak initial mixed layer stratification and reaches the base of the mixed layer in about 14 h. Figure 4 shows the evolution of the horizontally averaged potential density $\langle \sigma_t \rangle$ as a function of depth and time (top row) and the root-mean-square (rms)

vertical velocity calculated with respect to a horizontal average $\langle w'w' \rangle^{1/2}$ for Simulation A (left column) and Simulation B (right column). Here, potential density is calculated from the model buoyancy field using a reference density of 1024 kg m^{-3} .

Turbulent convection reaches a quasi-steady state in Simulation B, and the mixed layer gradually deepens. In this simulation the mean potential density is homogeneous in the mixed layer and the rms vertical velocity is nearly constant in time (except for statistical fluctuations) after the first day of simulation time. The mixed layer depth, diagnosed as the location where the horizontally averaged potential density is 0.01 kg m^{-3} larger than the surface value, gradually deepens in time in response to the surface forcing.

In Simulation A, stable stratification develops in the mixed layer after about 1 day. The mixed layer depth shoals briefly at $t \simeq 3$ days, which, as we will see below, corresponds to the development of a submesoscale eddy through baroclinic instability. The rms vertical velocity increases during this restratification event. After 4 days, the flow reaches a new statistically steady state. Notably, after this time there is a persistent stable stratification throughout the mixed layer and the rms vertical velocity is significantly reduced compared to Simulation B. The mixed layer depth, $h(t)$, is somewhat shallower at the end of Simulation A ($h \simeq 290 \text{ m}$) compared to the initial time ($h \simeq 315 \text{ m}$ using the criteria of $\Delta \sigma_t = 0.01 \text{ kg m}^{-3}$).

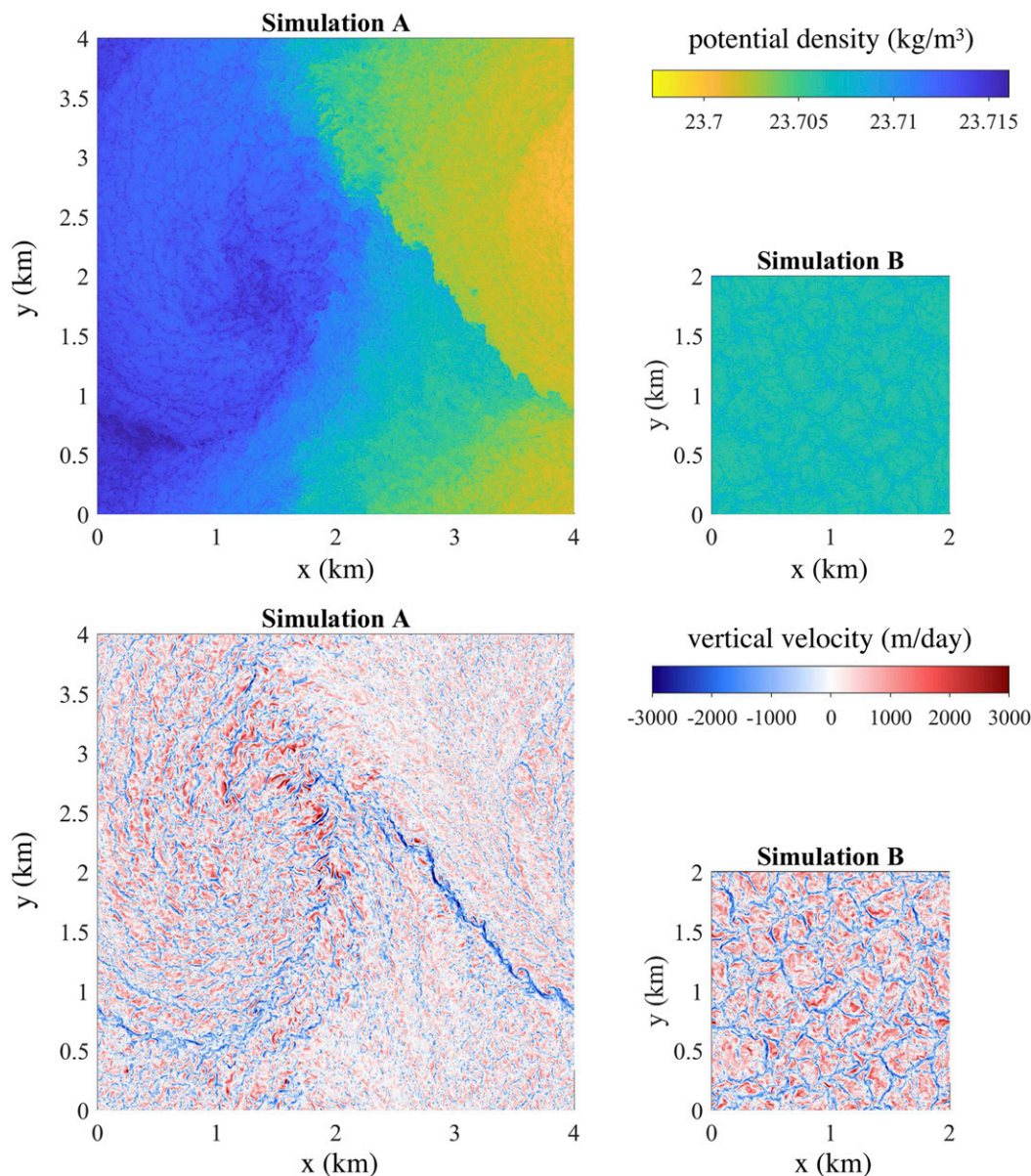


FIG. 5. Horizontal slices of (top) potential density and (bottom) vertical velocity for (left) Simulation A and (right) Simulation B at $t = 5$ days. In both cases the location of the horizontal slices is $z = -15.6$ m.

Note, however, that these values are sensitive to the definition of the mixed layer depth. For example, if the mixed layer were instead defined as the location where the stratification is half of the value in the thermocline, this depth would increase throughout Simulation A.

Horizontal slices of potential density and vertical velocity at a depth of 15.6 m and $t = 5$ days are shown in Fig. 5. In Simulation A, a submesoscale eddy is visible near the center of the domain with a diameter of 2–3 km. Relatively small convective cells are also visible within the submesoscale eddy and in the surrounding water. Outside of the eddy, horizontally convergent flow

generates a sharp submesoscale density front where the vertical velocity exceeds 3000 m day^{-1} ($\sim 3.5 \text{ cm s}^{-1}$). Note that the vertical velocity along the submesoscale front is more than one order of magnitude larger than typical values in simulations with a horizontal resolution of 1 km (e.g., Mahadevan and Tandon 2006; Capet et al. 2008; Bachman et al. 2017). The thinness of the submesoscale front suggests that very high resolution is needed to capture the largest vertical velocity. In Simulation B the signature of convection cells, with narrow regions of downwelling and broad regions of weaker upwelling, can be seen in the vertical velocity

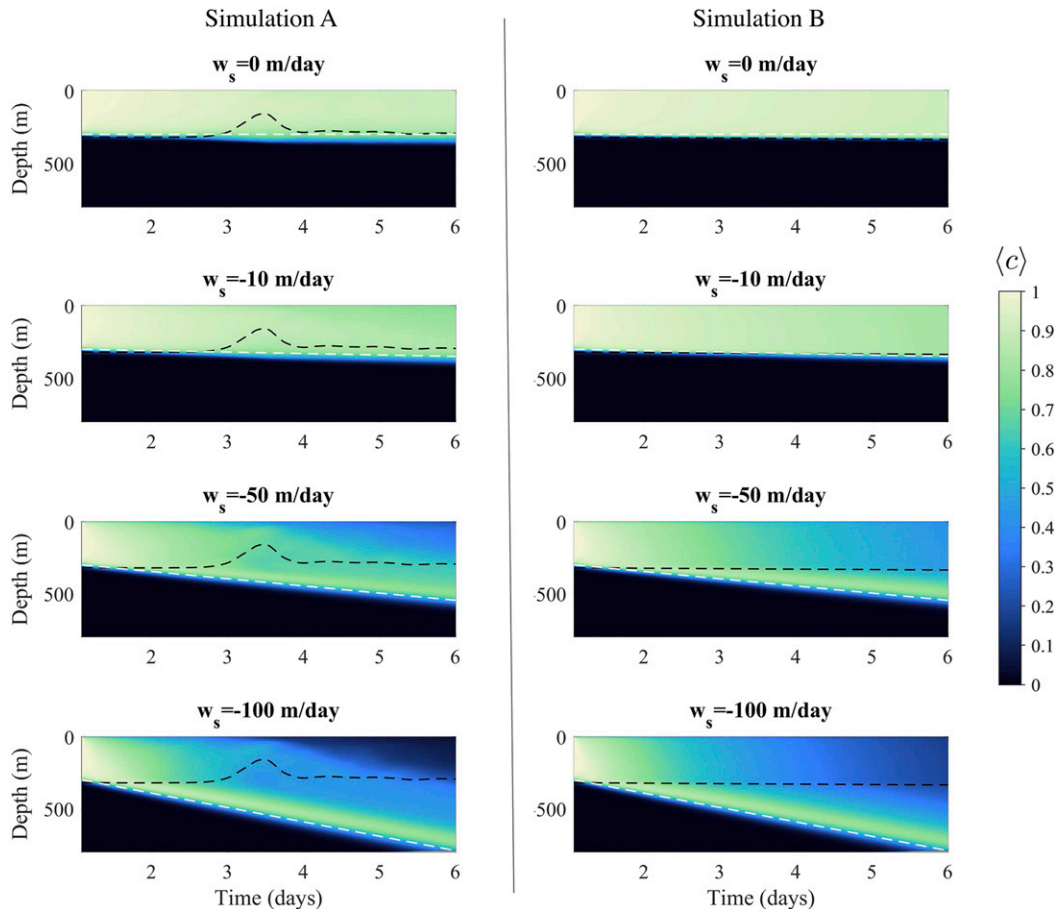


FIG. 6. Horizontally averaged particle concentration as a function of depth and time. The black dashed line shows the mixed layer depth as defined in Fig. 4. The slope of the white dashed line is equal to the sinking speed w_s .

slices. The convection cells are generally larger in Simulation B than in Simulation A.

Figure 6 shows the horizontally averaged particle concentration as a function of time and depth. The black dashed line shows the mixed layer depth using the same criteria as defined above, while the slope of the white line matches the sinking speed for each particle class. In Simulations A and B, the particle concentrations with $w_s = 0$ and $w_s = -10 \text{ m day}^{-1}$ remain relatively well mixed in the upper 300 m. Although difficult to see on the full depth axis shown in Fig. 6, the neutral tracer with $w_s = 0$ deepens more quickly in Simulation A than in Simulation B. Just after the saturation of MLI at 3.5 days, the depth where the mean tracer concentration is 0.5 is about 335 m in Simulation A and 320 m in Simulation B. This indicates enhanced subduction of the neutral tracer by submesoscales as seen in Omand et al. (2015), although here the effect is modest.

For the more rapidly sinking particles, the mean particle concentration in the mixed layer is relatively uniform in Simulation B but is depth dependent in Simulation A.

The concentration of particles with $w_s = -100 \text{ m day}^{-1}$ in the mixed layer is smaller at the end of Simulation A compared to Simulation B, indicating that net export has been enhanced by submesoscales. There is also a brief resuspension event in Simulation A during the period when the mixed layer depth shoals ($t = 3\text{--}4$ days), causing the mixed layer particle concentration in Simulation A to briefly exceed that in Simulation B (not shown). The export rate will be analyzed quantitatively below. To a good approximation, the mean particle concentration is unchanged as it translates down through the thermocline with a speed set by the settling velocity w_s .

b. Particle concentration and mixing

Vertical profiles of the horizontally averaged particle concentration are shown in Fig. 7 for $t = 5$ days. Here, the depth dependence of the mixed layer particle concentration in Simulation A stands in contrast to the nearly uniform particle concentration in Simulation B. The profiles of particle concentration in Simulation B

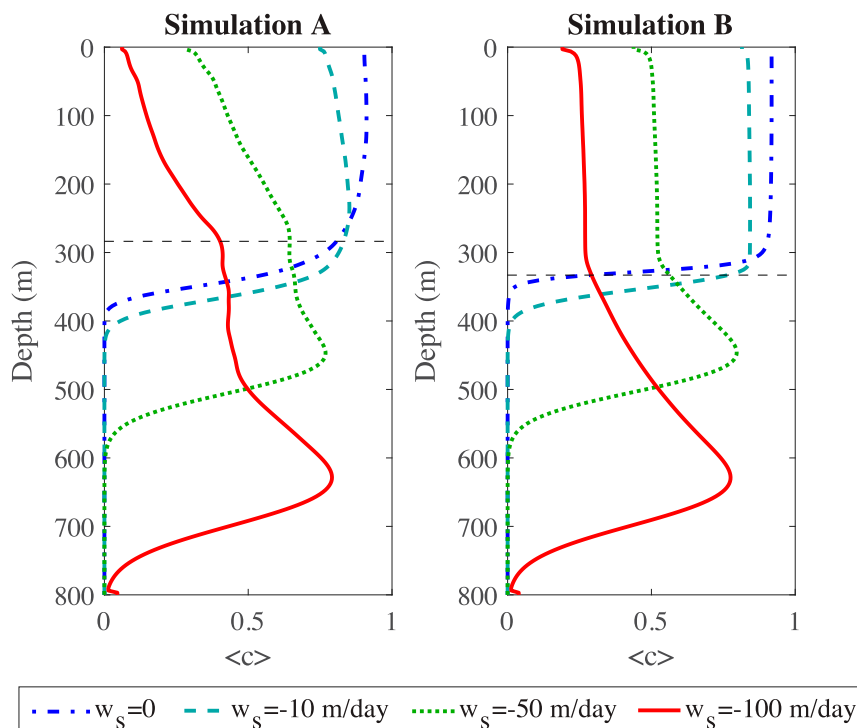


FIG. 7. Vertical profiles of the horizontally averaged particle concentration at $t = 5$ days for (left) Simulation A and (right) Simulation B. The particle concentration is normalized by the concentration in the mixed layer at $t = 0$. The thin dashed black line indicates the mixed layer depth in each case, defined using a density difference of 0.01 kg m^{-3} .

are qualitatively similar to the results reported in Noh et al. (2006), where Lagrangian particles were tracked in an LES of turbulent convection.

In addition to altering the mean particle concentration, submesoscales also generate strong horizontal variability in the particle concentration. This is illustrated in Fig. 8, which shows the concentrations of the most rapidly sinking particles ($w_s = -100 \text{ m day}^{-1}$) at the same time as in Fig. 5. The top panels show the particle concentration at $z = -150 \text{ m}$. Note that since the initial particle concentration was uniform in the upper 300 m, the horizontal variability is generated dynamically. The outline of the submesoscale eddy is visible in the particle concentration with low concentration near the center of the eddy and streaks of higher concentration encircling the eddy at this depth. In contrast, the particle concentration in Simulation B is much more homogeneous with relatively small fluctuations mirroring the pattern of convective cells.

As seen in the bottom-left panel in Fig. 8, submesoscale variability in the tracer concentration persists into the thermocline in Simulation A. This variability appears to be generated within or just below the mixed layer. This can be seen in Fig. 9, where the right panel shows the tracer variance production rate for Simulation

A, $-\langle w'c' \rangle \partial \langle c \rangle / \partial z$, where angle brackets represent an average in both horizontal directions and in time from the initialization of the tracer until $t = 6$ days. There is a peak in the tracer variance production at the base of the mixed layer for $w_s = 0, -10 \text{ m day}^{-1}$, while the tracer variance production is maximum near the surface for $w_s = -50, -100 \text{ m day}^{-1}$. In all cases, the variance production is small below about $z = -350 \text{ m}$.

Vertical advection plays a qualitatively different role for neutrally buoyant and sinking particles in Simulation A. This can be seen in the left panel of Fig. 9, which shows the resolved component of the vertical advective particle concentration flux, averaged in the horizontal directions and in time from 26 h (when the particle concentration was initialized) to 6 days for this simulation. For the neutrally buoyant tracer ($w_s = 0$), the advective flux is negative, indicating net *subduction*. However, for $w_s = -50, -100 \text{ m day}^{-1}$, the advective flux is positive, indicating net *upwelling*. In these cases the particle concentration increases with depth in the mixed layer (Fig. 7) and a positive advective flux is downgradient with respect to the mean concentration profile.

The depth dependence that develops in the mean particle concentration in Simulation A (see Figs. 6 and 7) can be explained by a reduction in vertical mixing

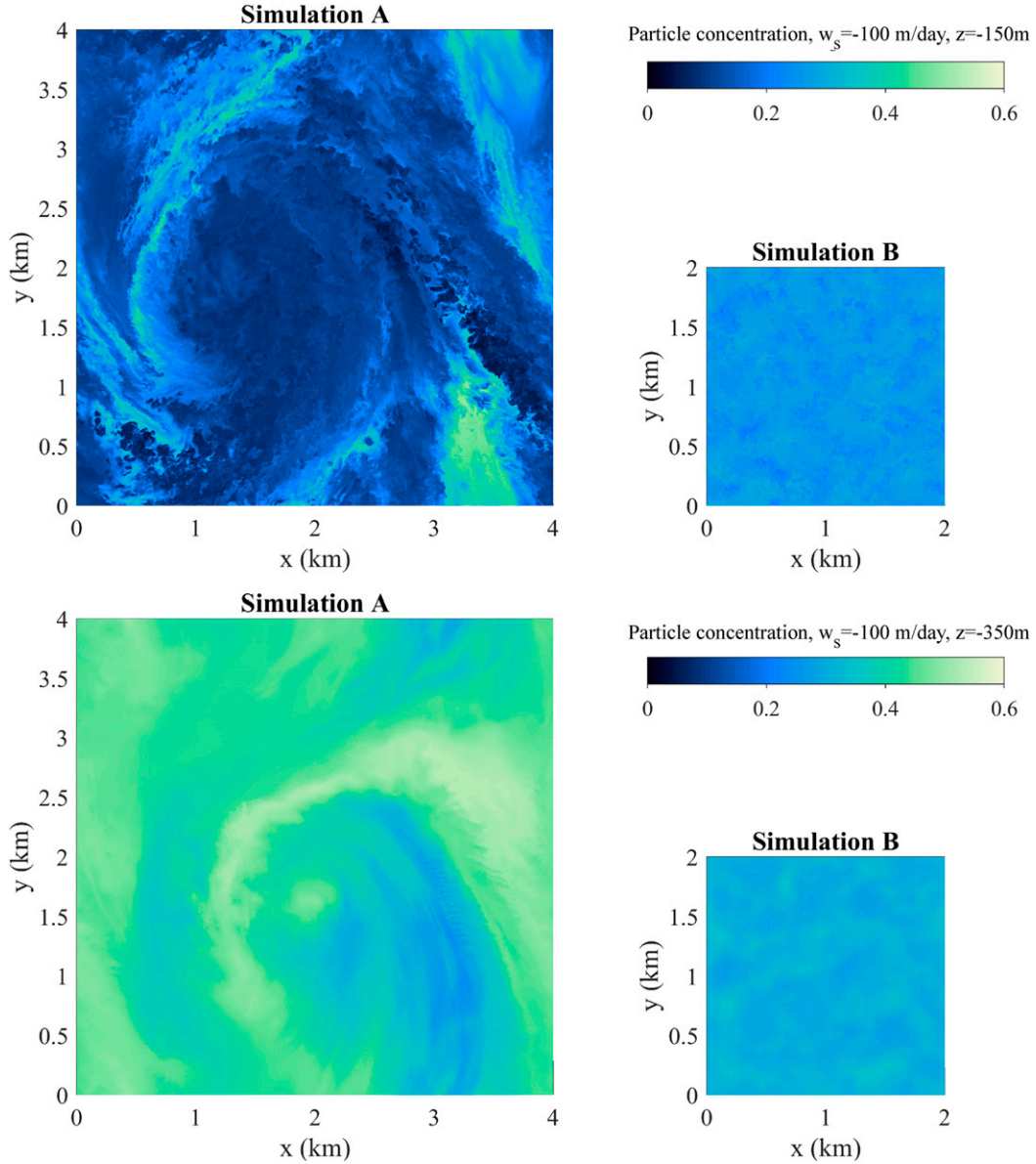


FIG. 8. Horizontal slices of particle concentration with a sinking velocity of $w_s = -100 \text{ m day}^{-1}$ for (left) Simulation A and (right) Simulation B at $t = 5$ days. (top) Horizontal slices at $z = -150$ m in the middle of the mixed layer and (bottom) horizontal slices in the thermocline at $z = -350$ m.

following the development of submesoscales and re-stratification of the mixed layer. To show this, and to connect with the theory described in [section 2](#), we can diagnose the vertical turbulent diffusivity from the LES. To do this, we divide the resolved vertical advective flux of particle concentration by the vertical concentration gradient, that is,

$$\kappa_T \equiv \frac{-\langle w'c' \rangle}{\frac{\partial \langle c \rangle}{\partial z}}, \quad (33)$$

and this quantity is shown in [Fig. 10](#) along with the subgrid-scale diffusivity. It is worth noting that κ_T includes contributions from submesoscales and small-scale turbulence. In [section 4d](#) we will identify the relative contribution of these components to the vertical fluxes.

The resolved diffusivity becomes undefined when the mean vertical tracer gradient is zero. In [Fig. 10](#), we only show the resolved diffusivity above the first zero crossing in the mean vertical tracer gradient in the upper 300 m since the diffusivity associated with the more slowly sinking tracers is not well defined in the thermocline.

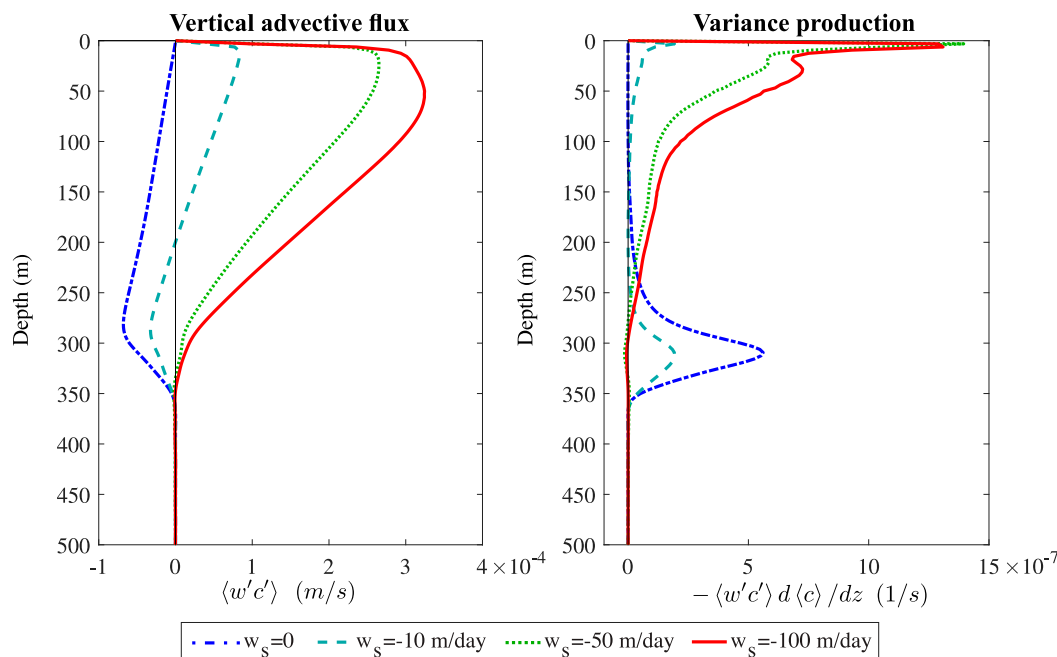


FIG. 9. (left) Vertical advective particle concentration flux and (right) production of particle concentration variance for Simulation A. Here angle brackets denote an average in both horizontal directions and in time from $t = 26$ h to $t = 6$ days.

In both simulations the subgrid-scale diffusivity is at least an order of magnitude smaller than the resolved diffusivity, indicating that the vertical tracer flux is dominated by the resolved contributions.

Interestingly, the turbulent diffusivity is not very sensitive to w_s . This stands in contrast to the conclusions from Taylor (2018) where it was found that the diffusivity was strongly dependent on the slip velocity for buoyant tracers. It is not immediately clear why this difference exists. If the base of the mixed layer were replaced with a rigid lid, buoyant and dense particles should be symmetric with respect to the top and bottom of the mixed layer. One possible explanation for the difference is that here sinking particles can sink across the base of the mixed layer, whereas buoyant particles tend to accumulate at the ocean surface where their vertical velocity relative to the fluid necessarily must vanish. Taylor (2018) found that buoyant tracers rose to the surface and then accumulated in regions of strong horizontal convergence and downwelling. If dense particles sink into the thermocline before they can accumulate in regions of strong upwelling, this could explain the lack of enhancement in the vertical diffusivity. Another possible explanation is the asymmetry in submesoscale frontogenesis. Frontogenesis is known to be more effective at the ocean surface where $w = 0$ (with the rigid lid approximation) than at the mixed layer base, and subduction at submesoscale fronts

tends to be stronger than upwelling (Mahadevan and Tandon 2006).

The turbulent diffusivity diagnosed for Simulation A is more than a factor of 10 smaller than the corresponding value in Simulation B. Since the initial conditions and forcing are the same in these simulations, the implication is that submesoscale restratification suppresses vertical mixing. This was also seen by Taylor (2016) and the degree of reduction in κ_T is broadly consistent with what was seen in that study for the same value of R_{MLI} [defined in Eq. (27)], although the reduction is somewhat stronger here. Note the mixed layer depth in Taylor (2016) was 50 m, significantly shallower than the value here. As we will show in the next section, the reduction in κ_T has significant implications for the rate of particle export.

In the thermocline, the resolved components of the diffusivity are small ($\sim 10^{-5} \text{ m}^2 \text{ s}^{-1}$) (not shown). The subgrid-scale diffusivity decreases throughout the thermocline and is about $3 \times 10^{-4} \text{ m}^2 \text{ s}^{-1}$ at the base of the computational domain in both simulations (not shown). The fact that the subgrid-scale diffusivity exceeds the resolved diffusivity in the thermocline implies that the simulations are not resolved in this region. Since the simulations do not have a background internal wave field, the motions in the thermocline are dominated by small-scale internal waves generated by dynamics in the upper part of the computational domain. The subgrid-scale

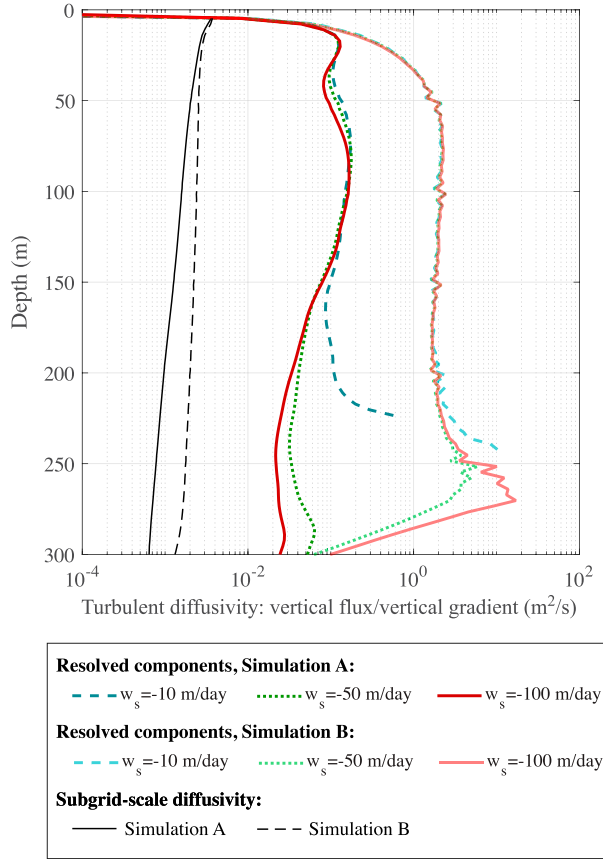


FIG. 10. Diagnosed turbulent diffusivity from the LES for Simulation A (solid curves) and Simulation B (dashed curves). The resolved component is calculated by dividing the mean vertical tracer flux by the mean vertical tracer gradient, where the average is applied over both horizontal directions and from $t = 4.5$ – 5.5 days. The subgrid-scale components show the mean subgrid-scale diffusivity with the same averaging window. Note that the vertical axis is confined to the approximate mixed layer depth and the diffusivity is only plotted above the first location where the mean vertical tracer gradient is zero.

model responds to these small-scale internal waves. We anticipate that the subgrid-scale diffusivity in the thermocline would decrease with increasing model resolution, although we are not able to test this here due to the large computational cost of the simulations. The elevated subgrid-scale diffusivity will lead to spurious mixing in the thermocline, and the tracer variability in the thermocline is therefore likely underestimated in the model.

c. Comparison between LES and theory

In this section we compare predictions from the theory described in section 2 with the LES results. Specifically, we diagnose the mean export rate from the simulations using

$$E = \frac{\frac{d}{dt} \int_{-h}^0 \langle c \rangle dz}{\int_{-h}^0 \langle c \rangle dz}. \quad (34)$$

This is compared with the export rate predicted by the theory using values of the mixed layer depth and turbulent diffusivity characteristic of the LES. The theory in section 2 was derived assuming that the mixed layer depth is constant in time. Accordingly, we will set $h = 300$ m when evaluating the theory in this section.

In the models described here, changes in the mixed layer depth do not appear to have a significant impact on the export rate. Although the mixed layer briefly shoals in Simulation A (as defined using a density difference of 0.01 kg m^{-3}) during the development of the submesoscale eddies, the mixed layer deepens again before the particles leave this region (see Fig. 6). While a constant surface forcing is applied here, changes in the mixed layer depth are likely to play an important role in the export and resuspension of sinking particles (e.g., D’Asaro 2008; Gardner et al. 1995). An extension to the theory to include a variable mixed layer depth is left to future work where it can be tested using appropriate simulations and/or observations.

For values characterizing Simulation B, specifically a turbulent diffusivity $\kappa = 2 \text{ m}^2 \text{ s}^{-1}$ and a mixed layer depth $h = 300$ m, the nondimensional turbulent velocity ratio is $T = w_*/w_s = (-57.6, -11.5, -5.8)$ for $w_s = (-10, -50, -100) \text{ m day}^{-1}$, respectively. Equation (17) then gives $r = (-115.4, -23.2, -11.8)$ [taking the $(-)$ branch which satisfies $r < -1$ as required for positive particle concentration]. Since $|r| \gg 1$ for all three values of w_s , the theory predicts that the particle concentration profiles will remain nearly depth independent in the mixed layer. This is consistent with the mean tracer profiles shown in Fig. 7. In this limit of strong mixing, the predicted export rate is $E \simeq |w_s|/h$, which is also in good agreement with the export rate diagnosed from the simulations (not shown).

The turbulent diffusivity in Simulation A is comparable to Simulation B *before* the submesoscale restratification event at $t \simeq 3$ days, while after this time the turbulent diffusivity decreases to the values shown in Fig. 10. This time dependence is important for producing a quantitative match between the simulations and the theory. To apply the theory to Simulation A, we use $\kappa = 2 \text{ m}^2 \text{ s}^{-1}$ for $t < 3$ days and $\kappa = 0.07 \text{ m}^2 \text{ s}^{-1}$ for $t > 3$ days (chosen based on the values in Fig. 10 at $z = -150$ m). The mixed layer depth in the theory is kept constant at $h = 300$ m. The initial conditions used in the theory are $c_0 = 1$ and $c_1 = 0$, matching the LES which was initialized with a uniform particle concentration in

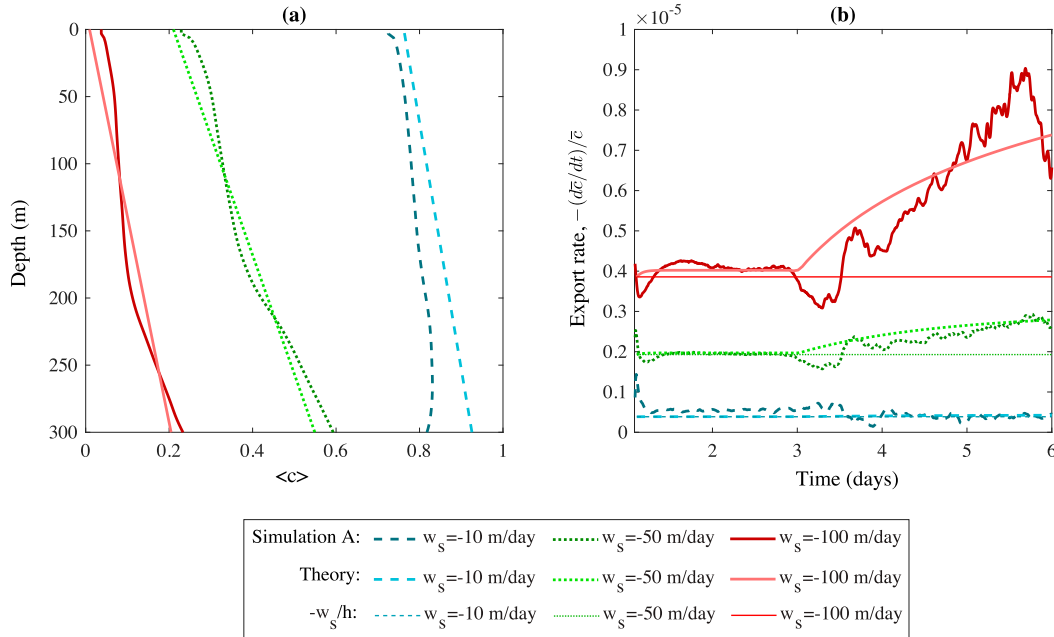


FIG. 11. Comparison between the theory described in section 2 and the LES model for Simulation A: (a) mean particle concentration profiles at $t = 6$ days and (b) mixed layer particle export rate. The thin lines in (b) show the export rate calculated from $-w_s/h$ that would result from a homogeneous mixed layer.

the mixed layer. Equations (7) and (9) are then time-stepped in MATLAB using the ode45 function. Note that the model results are somewhat sensitive to the values of κ and h , and while a detailed fit to the time-dependent κ and h from the simulations might yield a closer match, our objective is to test the ability of the theory to reproduce the qualitative features of the simulations.

Figure 11a shows horizontally averaged tracer profiles from Simulation A (thick lines and dark colors) and the profile obtained by solving Eqs. (7) and (9) (thin lines and light colors), both evaluated at $t = 6$ days. Note that only the mixed layer is shown. Both the average concentration and the vertical concentration gradient (represented in the theory by c_0 and c_1 , respectively) agree well.

Figure 11b shows a comparison between the export rate diagnosed in Simulation A and the prediction from the theory. The export rate is diagnosed from the simulation by first calculating the mean particle concentration in the mixed layer,

$$\bar{c}(t) = \frac{1}{h} \int_{-h}^0 \langle c \rangle dz, \quad (35)$$

where we have used $h = 300$ m. The export rate is then

$$E = -\frac{1}{\bar{c}} \frac{d\bar{c}}{dt}. \quad (36)$$

This is compared to the export rate from the theoretical model, specifically $E = -(dc_0/dt)/c_0$ from Eq. (20). For reference, we also show the export rate that would result if the particle concentration were uniform in the mixed layer, $E = -w_s/h$ (thin lines). For $t < 3$ days, before the restratification event, the simulated and theoretical export rates are close to $-w_s/h$. For $t > 3$ days, the reduction in κ leads to an increase in the export rate in Simulation A, which is broadly captured by the theory. The increase in the export rate is particularly notable for the tracer with $w_s = -100$ m day $^{-1}$ where it is enhanced by about a factor of 2 compared to the rate for a uniform distribution in the mixed layer.

d. Contribution of sub- and superinertial dynamics

As shown above, restratification by submesoscales reduces the vertical diffusivity which then enhances the export rate of sinking particles. The diffusivity defined in Eq. (33) is formed as the ratio of the vertical flux to the vertical gradient. A natural question is what fraction of the advective particle concentration flux $\langle w'c' \rangle$ can be attributed to subduction by submesoscales as opposed to small-scale turbulence. In this section, we attempt to decompose the vertical buoyancy flux and particle concentration flux in Simulation A into contributions from submesoscales and turbulence.

Previous studies have decomposed the contributions from submesoscales and small-scale turbulence in LES

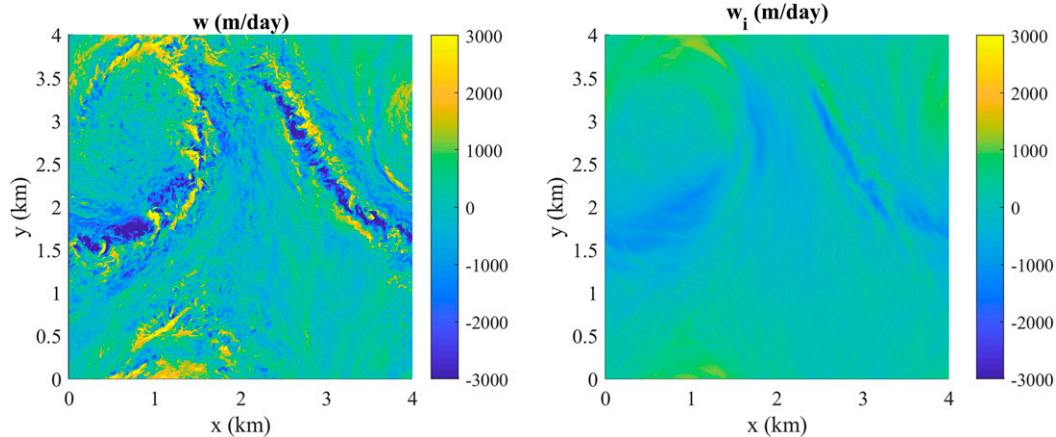


FIG. 12. (right) Filtered subinertial vertical velocity w_i averaged over the last inertial period of the simulation and (left) an instantaneous snapshot of the vertical velocity in the middle of the averaging window ($t = 5.83$ days). Both slices correspond to a depth of $z = -150$ m.

models using a spectral cutoff filter (e.g., Hamlington et al. 2014; Whitt and Taylor 2017). In these studies, there was a local minimum in the kinetic energy spectrum, which provided a natural choice for the cutoff wavenumber. The kinetic energy spectrum from Simulation A does not exhibit a local minimum, implying that there is not a scale separation between submesoscales and small-scale turbulence.

The simulations in Hamlington et al. (2014) and Whitt and Taylor (2017) included wind forcing and in both cases, the mixed layer was considerably shallower than our simulations. Here, convection in a deep mixed layer generates relatively large turbulent structures, as seen in Fig. 5 for Simulation B. At the same time, strong subduction occurs in a very narrow region along a submesoscale front in Simulation A. We hypothesize that the subduction at this front is driven by the submesoscale flow, even if it occurs within a region that is narrower than the submesoscale. Since the submesoscale front has a cross-front scale that is comparable to the convection cells, and since there is not a clear scale separation in the energy spectrum, it would be difficult to separate the contributions from submesoscales and convection using a spatial filter.

To overcome these difficulties, we decompose the contributions from submesoscales and small-scale turbulence using a *temporal* filter. Specifically, we decompose the vertical velocity into contributions from subinertial and superinertial motions, with the rationale that submesoscales generally vary on subinertial time scales, while small-scale turbulence is generally superinertial. To do this, we first save the model velocity on horizontal slices taken at $z = -150$ m. The velocity is saved about every 6 min of model time (although the exact interval varies throughout the

simulation along with the size of the adaptive time steps). These slices are then advected in a reference frame moving with the horizontal velocity averaged over each slice. The periodic boundary conditions ensure that boundary effects do not contaminate this process. A running time average with a length of one inertial period is then applied to define the “subinertial” vertical velocity according to

$$w_i(x, y, t) \equiv \frac{2\pi}{f} \int_{t-\frac{\pi}{f}}^{t+\frac{\pi}{f}} w(x, y, z = -150 \text{ m}, t') dt', \quad (37)$$

where f is the Coriolis frequency. The superinertial velocity is then defined to be $w^i = w - w_i$.

After calculating the subinertial and superinertial vertical velocity, w_i and w^i , we then decompose the vertical tracer flux into subinertial and superinertial contributions according to

$$\langle w'c' \rangle = \langle w_i c' \rangle + \langle w^i c' \rangle, \quad (38)$$

where again $\langle \cdot \rangle$ denotes a horizontal average. Note that the particle concentration is not filtered in the same way as the velocity. It would be possible to similarly calculate the subinertial and superinertial contributions to the tracer concentration, but this would result in four terms contributing to the flux and would complicate the physical interpretation.

Figure 12 shows a snapshot of the vertical velocity at $z = -150$ m at $t = 5.83$ days (left panel) and the subinertial vertical velocity w_i (right panel) where the averaging window used to construct w_i is centered on the time shown in the left panel. At this time the submesoscale eddy is centered in the upper-left quadrant of the panels. Small convective cells that appear inside the submesoscale

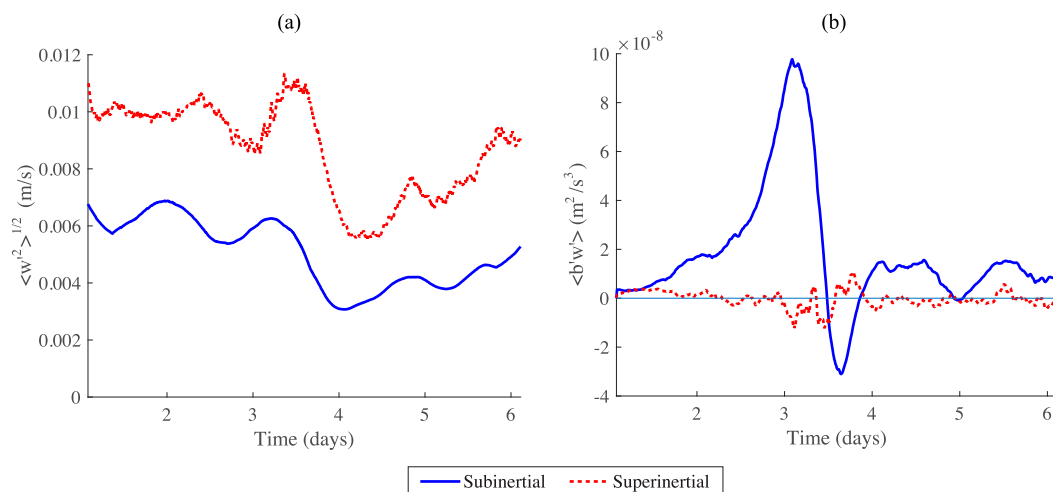


FIG. 13. Decomposition of (a) rms vertical velocity and (b) buoyancy flux into sub- and superinertial components using the method described in the text. The quantities are evaluated at a depth of 150 m, approximately in the middle of the mixed layer.

eddy in the instantaneous snapshot are removed by the subinertial filter. The subinertial vertical velocity is largest along the submesoscale front around the outside of the submesoscale eddy. The subinertial filter has the effect of removing most of the small-scale turbulence while preserving the velocity associated with the submesoscale eddy and the submesoscale front.

Figure 13a shows the rms of the subinertial and superinertial vertical velocity, w_i and w^i , calculated with respect to a horizontal average at $z = -150$ m. The superinertial rms vertical velocity is roughly twice as large as the subinertial component, indicating that relatively fast processes (e.g., convection) contribute significantly to the vertical circulation. In comparison to the rms vertical velocity, the subinertial component makes a much larger fractional contribution to the buoyancy flux (see Fig. 13b). Near the start of the simulation, both components make similar contributions to the buoyancy flux. However, the subinertial component of the buoyancy flux rapidly grows before reaching a maximum at $t \simeq 3$ days. This immediately precedes the restratification event seen in Fig. 4 and the large subinertial buoyancy flux indicates a transfer of potential energy to kinetic energy during the development of the submesoscale eddy through baroclinic instability.

Figure 14 shows the decomposition of the advective particle concentration flux at $z = -150$ m into subinertial and superinertial components using the method described above. The sign of the subinertial particle flux at this depth is consistent with the flux profiles shown in Fig. 9. For the most rapidly sinking particles, with $w_s = -50$ and $w_s = -100$ m day⁻¹, the superinertial component of the particle concentration flux gradually decreases as stratification develops in the mixed layer,

consistent with the suppression of vertical mixing as noted above. There is a large subinertial particle concentration flux in these cases at a time corresponding to the maximum subinertial buoyancy flux. This can be interpreted as resuspension of the sinking particles during the development of the submesoscale eddy.

5. Discussion

Previous studies have found that submesoscales can enhance the export flux through direct subduction (e.g., Omand et al. 2015; Liu et al. 2018). Here, we decomposed the advective particle concentration flux into sub and superinertial components as a proxy for submesoscale and turbulent motions. As shown in Fig. 14, subinertial motions induce a negative (downward) advective flux for the neutral tracer ($w_s = 0$) which is maximum at $t \simeq 3$ days as the submesoscale eddy develops. This is qualitatively consistent with the findings from Omand et al. (2015). For the fastest sinking tracers ($w_s = -50, -100$ m day⁻¹), the subinertial advective flux at this time is positive, indicating resuspension of the particles. This is consistent with previous work showing that submesoscales enhance the upward transport of tracers (including biological nutrients) with a maximum concentration below the mixed layer (Lévy et al. 2012; Mahadevan 2016). As noted by Smith et al. (2016), the response of tracers to submesoscale motions depends on their vertical distribution.

We did not include any terms accounting for sources or sinks of particles and instead simulate an instantaneous injection of particles, distributed uniformly throughout the mixed layer. The enhancement in export associated with particle settling seen here can be linked with a

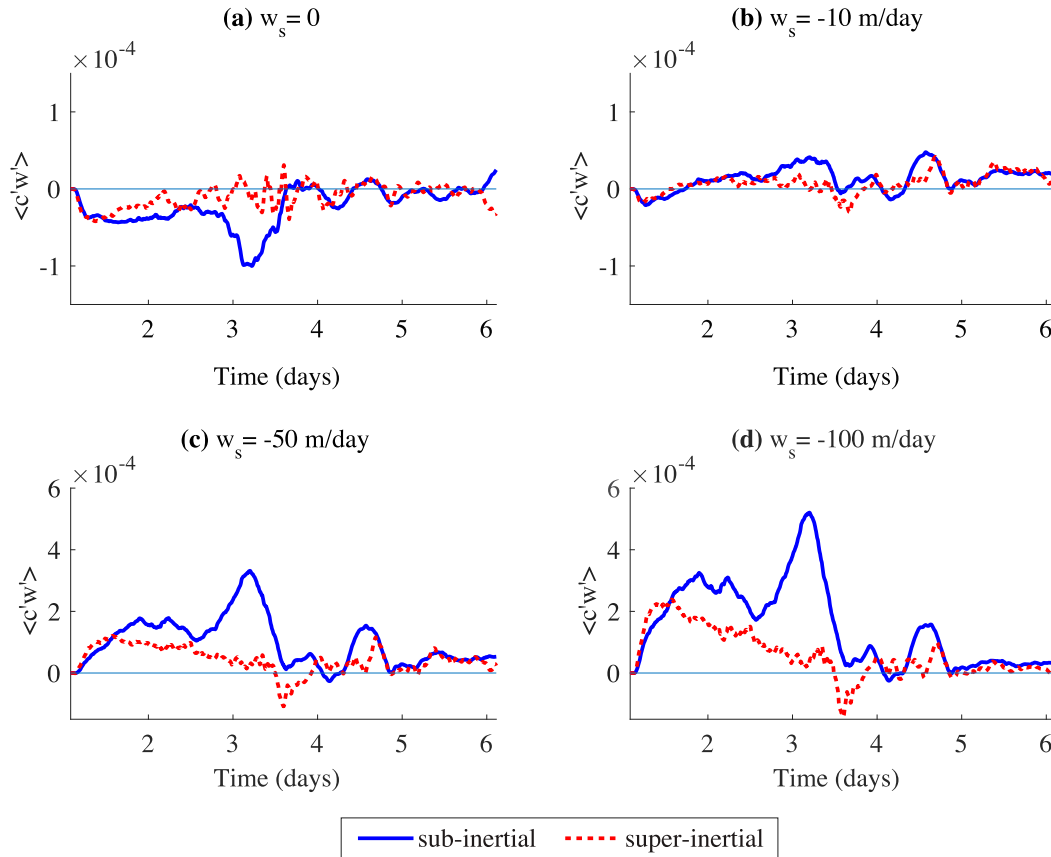


FIG. 14. Decomposition of the vertical advective concentration flux at $z = -150$ m into sub- and superinertial components using the method described in the text. Note that a different scale is used for the y axis in the top and bottom rows.

depth-dependent particle concentration profile in the mixed layer. To the extent that the mixed layer particle concentration increases with depth in the presence of a continuous source of particles, we anticipate that reduced vertical mixing will enhance the export rate. However, if the particle concentration is surface intensified, reduced vertical mixing could have the opposite effect. These predictions could be tested using observations or more realistic simulations.

The mechanism described here is distinct from the mixed layer pump that has been described in several previous studies (e.g., Gardner et al. 1995; Bol et al. 2018; Dall’Omo et al. 2016). According to the concept of the mixed layer pump described by Gardner et al. (1995), when the mixed layer deepens, small particles are advected to the base of the mixed layer more quickly than they would move through gravitational settling alone. After a shoaling of the mixed layer (e.g., through diurnal solar insolation), some of the particles are left behind in relatively quiescent water at the bottom of the former mixed layer. Some of these particles then have time to sink into the thermocline before the next mixed layer deepening event.

Here, the restratification induced by submesoscales occurs throughout the mixed layer. The stratification is strong enough to significantly reduce the rate of vertical mixing, but vertical advective fluxes of the particles remain (both due to superinertial and subinertial motions as shown in Fig. 14). The dichotomy between a highly turbulent, homogeneous mixed layer overlying a quiescent region does not accurately describe this situation. Indeed, it was noted by Gardner et al. (1995) that the definition of the mixed layer depth is often arbitrary and that sometimes an iso-property “mixed” layer does not exist.

In Simulation A, the mixed layer depth defined using a density difference of 0.01 kg m^{-3} starts at about 320 m and decreases briefly during the development of the submesoscale eddy at $t \simeq 3.5$ days before deepening again to about 290 m. The normalized export rate is not significantly enhanced during the brief period when the mixed layer depth shoals, as would be expected based on the mixed layer pump mechanism. In fact during this period, the densest particles are fluxed upward by sub-inertial (submesoscale) motions.

6. Conclusions

We have studied the influence of submesoscales and convective turbulence on the concentration and export of sinking particles. We found that **restratification by submesoscales reduces the strength of vertical mixing, thereby enhancing particle export associated with gravitational settling.** To our knowledge, this is the first time that this mechanism has been described.

We used large-eddy simulations to study the interaction between submesoscale dynamics and small-scale turbulence and their influence on particle export. The simulations each started with a 300-m-deep mixed layer and were forced by cooling the surface with an imposed buoyancy flux, equivalent to a heat flux of roughly -150 W m^{-2} . One simulation included a background horizontal density gradient in a “frontal zone” configuration and the other did not.

In the simulation with a front, submesoscales developed after about 2 days, leading to an increase in the stratification within the mixed layer. Despite the constant imposed surface cooling, the rate of vertical mixing decreased significantly after the restratification event. **For particles sinking at speeds of -50 and -100 m day^{-1} , the reduced rate of mixing led to a depth-dependent particle concentration in the mixed layer, with larger concentrations near the mixed layer base.** More particles were then able to escape the mixed layer through gravitational settling, increasing the export rate.

It is worth noting that the surface forcing is constant in the simulations shown here. If time-dependent forcing were used (e.g., a variable wind stress or a diurnal cycle), the mixed layer depth would likely have changed more dramatically in time. It should be possible to extend the theory presented in [section 2](#) to allow a time-dependent mixed layer depth. This would combine the mixed layer pump and incomplete mixing mechanisms into a single framework.

Acknowledgments. The authors would like to thank Amala Mahadevan and an anonymous referee for very helpful comments on the paper.

REFERENCES

- Abkar, M., and P. Moin, 2017: Large-eddy simulation of thermally stratified atmospheric boundary-layer flow using a minimum dissipation model. *Bound.-Layer Meteor.*, **165**, 405–419, <https://doi.org/10.1007/s10546-017-0288-4>.
- , H. J. Bae, and P. Moin, 2016: Minimum-dissipation scalar transport model for large-eddy simulation of turbulent flows. *Phys. Rev. Fluids*, **1**, 041701, <https://doi.org/10.1103/PHYSREVFLUIDS.1.041701>.
- Bachman, S. D., J. Taylor, K. Adams, and P. Hosegood, 2017: Mesoscale and submesoscale effects on mixed layer depth in the Southern Ocean. *J. Phys. Oceanogr.*, **47**, 2173–2188, <https://doi.org/10.1175/JPO-D-17-0034.1>.
- Boccaletti, G., R. Ferrari, and B. Fox-Kemper, 2007: Mixed layer instabilities and restratification. *J. Phys. Oceanogr.*, **37**, 2228–2250, <https://doi.org/10.1175/JPO3101.1>.
- Bol, R., S. A. Henson, A. Rumyantseva, and N. Briggs, 2018: High-frequency variability of small-particle carbon export flux in the Northeast Atlantic. *Global Biogeochem. Cycles*, **32**, 1803–1814, <https://doi.org/10.1029/2018GB005963>.
- Buckingham, C. E., and Coauthors, 2016: Seasonality of submesoscale flows in the ocean surface boundary layer. *Geophys. Res. Lett.*, **43**, 2118–2126, <https://doi.org/10.1002/2016GL068009>.
- Burd, A. B., and G. A. Jackson, 2009: Particle aggregation. *Annu. Rev. Mar. Sci.*, **1**, 65–90, <https://doi.org/10.1146/annurev.marine.010908.163904>.
- Callies, J., and R. Ferrari, 2018: Baroclinic instability in the presence of convection. *J. Phys. Oceanogr.*, **48**, 45–60, <https://doi.org/10.1175/JPO-D-17-0028.1>.
- Capet, X., J. C. McWilliams, M. J. Molemaker, and A. Shchepetkin, 2008: Mesoscale to submesoscale transition in the California Current System. Part I: Flow structure, eddy flux, and observational tests. *J. Phys. Oceanogr.*, **38**, 29–43, <https://doi.org/10.1175/2007JPO3671.1>.
- Chisholm, S. W., 2000: Oceanography: Stirring times in the Southern Ocean. *Nature*, **407**, 685–686, <https://doi.org/10.1038/35037696>.
- Dall’Omo, G., J. Dingle, L. Polimene, R. J. Brewin, and H. Claustre, 2016: Substantial energy input to the mesopelagic ecosystem from the seasonal mixed-layer pump. *Nat. Geosci.*, **9**, 820–823, <https://doi.org/10.1038/ngeo2818>.
- D’Asaro, E. A., 2008: Convection and the seeding of the North Atlantic bloom. *J. Mar. Syst.*, **69**, 233–237, <https://doi.org/10.1016/j.jmarsys.2005.08.005>.
- Eppley, R. W., and B. J. Peterson, 1979: Particulate organic matter flux and planktonic new production in the deep ocean. *Nature*, **282**, 677–680, <https://doi.org/10.1038/282677a0>.
- Erickson, Z. K., and A. F. Thompson, 2018: The seasonality of physically driven export at submesoscales in the northeast Atlantic Ocean. *Global Biogeochem. Cycles*, **32**, 1144–1162, <https://doi.org/10.1029/2018GB005927>.
- Fennel, K., I. Cetinić, E. D’Asaro, C. Lee, and M. Perry, 2011: Autonomous data describe North Atlantic spring bloom. *Eos, Trans. Amer. Geophys. Union*, **92**, 465–466, <https://doi.org/10.1029/2011EO500002>.
- Fox-Kemper, B., R. Ferrari, and R. Hallberg, 2008: Parameterization of mixed layer eddies. Part I: Theory and diagnosis. *J. Phys. Oceanogr.*, **38**, 1145–1165, <https://doi.org/10.1175/2007JPO3792.1>.
- Gardner, W. D., S. P. Chung, M. J. Richardson, and I. D. Walsh, 1995: The oceanic mixed-layer pump. *Deep-Sea Res.*, **42**, 757–775, [https://doi.org/10.1016/0967-0645\(95\)00037-Q](https://doi.org/10.1016/0967-0645(95)00037-Q).
- Hamlington, P. E., L. P. Van Roekel, B. Fox-Kemper, K. Julien, and G. P. Chini, 2014: Langmuir–submesoscale interactions: Descriptive analysis of multiscale frontal spindown simulations. *J. Phys. Oceanogr.*, **44**, 2249–2272, <https://doi.org/10.1175/JPO-D-13-0139.1>.
- Henson, S. A., R. Sanders, E. Madsen, P. J. Morris, F. Le Moigne, and G. D. Quartly, 2011: A reduced estimate of the strength of the ocean’s biological carbon pump. *Geophys. Res. Lett.*, **38**, L04606, <https://doi.org/10.1029/2011GL046735>.
- Klein, P., and G. Lapeyre, 2009: The oceanic vertical pump induced by mesoscale and submesoscale turbulence. *Annu. Rev. Mar. Sci.*, **1**, 351–375, <https://doi.org/10.1146/annurev.marine.010908.163704>.

- Large, W. G., J. C. McWilliams, and S. C. Doney, 1994: Oceanic vertical mixing: A review and a model with a nonlocal boundary layer parameterization. *Rev. Geophys.*, **32**, 363–403, <https://doi.org/10.1029/94RG01872>.
- Laws, E. A., P. G. Falkowski, W. O. Smith Jr., H. Ducklow, and J. J. McCarthy, 2000: Temperature effects on export production in the open ocean. *Global Biogeochem. Cycles*, **14**, 1231–1246, <https://doi.org/10.1029/1999GB001229>.
- Lévy, M., R. Ferrari, P. J. Franks, A. P. Martin, and P. Rivière, 2012: Bringing physics to life at the submesoscale. *Geophys. Res. Lett.*, **39**, L14602, <https://doi.org/10.1029/2012GL052756>.
- Liu, G., A. Bracco, and U. Passow, 2018: The influence of mesoscale and submesoscale circulation on sinking particles in the northern Gulf of Mexico. *Elem. Sci. Anth.*, **6**, 36, <https://doi.org/10.1525/ELEMENTA.292>.
- Mahadevan, A., 2016: The impact of submesoscale physics on primary productivity of plankton. *Annu. Rev. Mar. Sci.*, **8**, 161–184, <https://doi.org/10.1146/annurev-marine-010814-015912>.
- , and A. Tandon, 2006: An analysis of mechanisms for submesoscale vertical motion at ocean fronts. *Ocean Modell.*, **14**, 241–256, <https://doi.org/10.1016/j.ocemod.2006.05.006>.
- , —, and R. Ferrari, 2010: Rapid changes in mixed layer stratification driven by submesoscale instabilities and winds. *J. Geophys. Res.*, **115**, C03017, <https://doi.org/10.1029/2008JC005203>.
- , E. D’Asaro, C. Lee, and M. J. Perry, 2012: Eddy-driven stratification initiates North Atlantic spring phytoplankton blooms. *Science*, **337**, 54–58, <https://doi.org/10.1126/science.1218740>.
- McWilliams, J. C., 2016: Submesoscale currents in the ocean. *Proc. Roy. Soc.*, **A472**, 20160117, <https://doi.org/10.1098/RSPA.2016.0117>.
- Noh, Y., and S. Nakada, 2010: Estimation of the particle flux from the convective mixed layer by large eddy simulation. *J. Geophys. Res.*, **115**, C05007, <https://doi.org/10.1029/2009JC005669>.
- , I. Kang, M. Herold, and S. Raasch, 2006: Large eddy simulation of particle settling in the ocean mixed layer. *Phys. Fluids*, **18**, 085109, <https://doi.org/10.1063/1.2337098>.
- Omand, M. M., E. A. D’Asaro, C. M. Lee, M. J. Perry, N. Briggs, I. Cetinić, and A. Mahadevan, 2015: Eddy-driven subduction exports particulate organic carbon from the spring bloom. *Science*, **348**, 222–225, <https://doi.org/10.1126/science.1260062>.
- Resplandy, L., M. Lévy, and D. J. McGillicuddy Jr., 2019: Effects of eddy-driven subduction on ocean biological carbon pump. *Global Biogeochem. Cycles*, **33**, 1071–1084, <https://doi.org/10.1029/2018GB006125>.
- Rozema, W., H. J. Bae, P. Moin, and R. Verstappen, 2015: Minimum-dissipation models for large-eddy simulation. *Phys. Fluids*, **27**, 085107, <https://doi.org/10.1063/1.4928700>.
- Smith, K. M., P. E. Hamlington, and B. Fox-Kemper, 2016: Effects of submesoscale turbulence on ocean tracers. *J. Geophys. Res. Oceans*, **121**, 908–933, <https://doi.org/10.1002/2015JC011089>.
- Taylor, J. R., 2016: Turbulent mixing, restratification, and phytoplankton growth at a submesoscale eddy. *Geophys. Res. Lett.*, **43**, 5784–5792, <https://doi.org/10.1002/2016GL069106>.
- , 2018: Accumulation and subduction of buoyant material at submesoscale fronts. *J. Phys. Oceanogr.*, **48**, 1233–1241, <https://doi.org/10.1175/JPO-D-17-0269.1>.
- , and R. Ferrari, 2009: On the equilibration of a symmetrically unstable front via a secondary shear instability. *J. Fluid Mech.*, **622**, 103–113, <https://doi.org/10.1017/S0022112008005272>.
- , and —, 2010: Buoyancy and wind-driven convection at mixed layer density fronts. *J. Phys. Oceanogr.*, **40**, 1222–1242, <https://doi.org/10.1175/2010JPO4365.1>.
- , and —, 2011: Ocean fronts trigger high latitude phytoplankton blooms. *Geophys. Res. Lett.*, **38**, L23601, <https://doi.org/10.1029/2011GL049312>.
- Thomas, L. N., 2005: Destruction of potential vorticity by winds. *J. Phys. Oceanogr.*, **35**, 2457–2466, <https://doi.org/10.1175/JPO2830.1>.
- , A. Tandon, and A. Mahadevan, 2008: Submesoscale processes and dynamics. *Ocean Modeling in an Eddying Regime*, *Geophys. Monogr.*, Vol. 177, Amer. Geophys. Union, 17–38.
- , J. R. Taylor, E. A. D’Asaro, C. M. Lee, J. M. Klymak, and A. Shcherbina, 2016: Symmetric instability, inertial oscillations, and turbulence at the Gulf Stream front. *J. Phys. Oceanogr.*, **46**, 197–217, <https://doi.org/10.1175/JPO-D-15-0008.1>.
- Thompson, A. F., A. Lazar, C. Buckingham, A. C. Naveira Garabato, G. M. Damerell, and K. J. Heywood, 2016: Open-ocean submesoscale motions: A full seasonal cycle of mixed layer instabilities from gliders. *J. Phys. Oceanogr.*, **46**, 1285–1307, <https://doi.org/10.1175/JPO-D-15-0170.1>.
- Thorpe, S. A., 2005: *The Turbulent Ocean*. Cambridge University Press, 458 pp.
- Verstappen, R., 2018: How much eddy dissipation is needed to counterbalance the nonlinear production of small, unresolved scales in a large-eddy simulation of turbulence? *Comput. Fluids*, **176**, 276–284, <https://doi.org/10.1016/J.COMPFLUID.2016.12.016>.
- Vreugdenhil, C. A., and J. R. Taylor, 2018: Large-eddy simulations of stratified plane Couette flow using the anisotropic minimum-dissipation model. *Phys. Fluids*, **30**, 085104, <https://doi.org/10.1063/1.5037039>.
- Waite, A. M., and Coauthors, 2016: The wineglass effect shapes particle export to the deep ocean in mesoscale eddies. *Geophys. Res. Lett.*, **43**, 9791–9800, <https://doi.org/10.1002/2015GL066463>.
- Whitt, D. B., and J. R. Taylor, 2017: Energetic submesoscales maintain strong mixed layer stratification during an autumn storm. *J. Phys. Oceanogr.*, **47**, 2419–2427, <https://doi.org/10.1175/JPO-D-17-0130.1>.
- Yu, X., A. C. Naveira Garabato, A. P. Martin, C. E. Buckingham, L. Brannigan, and Z. Su, 2019: An annual cycle of submesoscale vertical flow and restratification in the upper ocean. *J. Phys. Oceanogr.*, **49**, 1439–1461, <https://doi.org/10.1175/JPO-D-18-0253.1>.